The Astronomical Journal, 164:159 (24pp), 2022 October https://doi.org/10.3847/1538-3881/ac83a9

Lyα Escape from Low-mass, Compact, High-redshift Galaxies

Ragadeepika Pucha[1], Naveen A. Reddy[2], Arjun Dey[3], Stéphanie Juneau[3], Kyoung-Soo Lee[4], Moire K. M. Prescott[5], Irene Shivaei[1], and Sungryong Hong[6]
[1] Steward Observatory, The University of Arizona, 933 North Cherry Avenue, Tucson, AZ 85721, USA; rpucha@arizona.edu
[2] Department of Physics & Astronomy, University of California, 900 University Avenue, Riverside, CA 92521, USA
[3] NSF's NOIRLab, 950 North Cherry Avenue, Tucson, AZ 85719, USA
[4] Department of Physics & Astronomy, Purdue University, 525 Northwestern Avenue, West Lafayette, IN 47907, USA
[5] Department of Astronomy, New Mexico State University, PO Box 30001, MSC 4500, Las Cruces, NM 88003, USA
[6] Korea Astronomy and Space Science Institute, 776 Daedeokdae-ro, Yuseong-gu, Daejeon 34055, Republic of Korea
Received 2022 May 5; revised 2022 July 6; accepted 2022 July 22; published 2022 September 26

Abstract

We investigate the effects of stellar populations and sizes on Lyα escape in 27 spectroscopically confirmed and 35 photometric Lyα emitters (LAEs) at $z \approx 2.65$ in seven fields of the Boötes region of the NOAO Deep Wide-Field Survey. We use deep HST/WFC3 imaging to supplement ground-based observations and infer key galaxy properties. Compared to typical star-forming galaxies (SFGs) at similar redshifts, the LAEs are less massive ($M_\star \approx 10^7$–$10^9\,M_\odot$), younger (ages $\lesssim$1 Gyr), smaller ($r_e < 1$ kpc), and less dust-attenuated ($E(B-V) \leqslant 0.26$ mag) but have comparable star formation rates (SFRs $\approx$ 1–100 $M_\odot$ yr^{-1}). Some of the LAEs in the sample may be very young galaxies having low nebular metallicities ($Z_{\rm neb} \lesssim 0.2\,Z_\odot$) and/or high ionization parameters ($\log(U) \gtrsim -2.4$). Motivated by previous studies, we examine the effects of the concentration of star formation and gravitational potential on Lyα escape by computing SFR surface density, $\Sigma_{\rm SFR}$, and specific SFR surface density, $\Sigma_{\rm sSFR}$. For a given $\Sigma_{\rm SFR}$, the Lyα escape fraction is higher for LAEs with lower stellar masses. The LAEs have a higher $\Sigma_{\rm sSFR}$, on average, compared to SFGs. Our results suggest that compact star formation in a low gravitational potential yields conditions amenable to the escape of Lyα photons. These results have important implications for the physics of Lyα radiative transfer and for the type of galaxies that may contribute significantly to cosmic reionization.

Unified Astronomy Thesaurus concepts: High-redshift galaxies (734); Star formation (1569); H II regions (694); Compact H II region (286)

Supporting material: extended figures

1. Introduction

The Lyα emission line of hydrogen is one of the strongest emission lines in the universe and is invaluable for selecting high-redshift sources (Partridge & Peebles 1967). Galaxies selected via this emission line (Lyα emitters, LAEs) are typically fainter in their continuum emission compared to galaxies selected using traditional Lyman break techniques (Lyman break galaxies, LBGs; Steidel & Hamilton 1993; Giavalisco 2002). Thus, LAEs probe the low-luminosity end of the galaxy luminosity function. They are also excellent tracers of large-scale structures in the universe (see Ouchi et al. 2020, and references therein).

Several deep narrowband imaging surveys have targeted LAEs in the past couple of decades. These include the Large Area Lyman Alpha survey (e.g., Rhoads et al. 2000), the Subaru deep survey (e.g., Ouchi et al. 2003), the Hobby–Eberly Telescope Dark Energy Experiment Pilot Survey (e.g., Adams et al. 2011), and the Multi Unit Spectroscopic Explorer Hubble Ultra Deep Field survey (e.g., Bacon et al. 2017). Due to their faint continua, these galaxies are often studied via stacking analysis (Gawiser et al. 2006; Finkelstein et al. 2007; Gawiser et al. 2007; Nilsson et al. 2007; Lai et al. 2008; Finkelstein et al. 2009; Ono et al. 2010; Guaita et al. 2011; Acquaviva et al. 2012; Vargas et al. 2014; Hao et al. 2018; Kusakabe et al. 2018), which can mask the intrinsic scatter in the distribution of LAE properties. Due to the availability of deep observations, it is now possible to study individual LAEs and their properties (Pirzkal et al. 2007; Nilsson et al. 2011; Hagen et al. 2014; McLinden et al. 2014; Vargas et al. 2014; Sandberg et al. 2015; Hathi et al. 2016; Shimakawa et al. 2017; Hao et al. 2018). These studies suggest that LAEs are typically low-mass, young, star-forming galaxies (SFGs) with low dust content. They are also considered to be important probes for studying low-mass galaxies that are the primary building blocks of typical present-day $L^\star$ galaxies (Gawiser et al. 2007; Hao et al. 2018; Khostovan et al. 2019; Herrero Alonso et al. 2021). Furthermore, morphological studies of LAEs have shown that they are compact (effective radius $r_e \approx 1$ kpc), and the sizes do not evolve with redshift (Bond et al. 2009, 2012; Gronwall et al. 2011; Malhotra et al. 2012; Paulino-Afonso et al. 2018; Shibuya et al. 2019).

Despite this progress, the resonant nature of Lyα emission poses many challenges in interpreting the observations (Dijkstra 2017). In fact, Lyα is often used to study the spatial structure of the interstellar medium (ISM) and circumgalactic medium in and around galaxies (Steidel et al. 2011; Momose et al. 2014; Wisotzki et al. 2018; Herenz et al. 2020; Leclercq et al. 2020; Sanderson et al. 2021). These photons can be easily scattered by neutral hydrogen (H I; column density $\gtrsim 10^{18}$ cm^{-2}) until they either "escape" the galaxy or get absorbed by dust. The fraction of Lyα photons that escape a galaxy, or the Lyα escape fraction ($f_{\rm esc}^{\rm Ly\alpha}$), is thus a complicated function of the spatial distribution

of H I gas (i.e., the gas covering fraction), gas kinematics, and dust (Kornei et al. 2010; Hayes et al. 2011; Wofford et al. 2013; Rivera-Thorsen et al. 2015; Trainor et al. 2015; Reddy et al. 2016; Jaskot et al. 2019). Understanding the physical mechanisms that alter the internal distribution of gas is therefore important to understand the physics of Lyα escape.

Comparing LAEs to continuum-selected SFGs can lend insight into the key factors regulating the escape of Lyα photons from galaxies. The Lyα measurements of SFGs have shown that some have observable Lyα emission, while others do not (Pentericci et al. 2007; Hathi et al. 2016; De Barros et al. 2017; Arrabal Haro et al. 2018, 2020; Du et al. 2018; Weiss et al. 2021). Several studies have measured $f_{\rm esc}^{\rm Ly\alpha}$ for LAEs and typical SFGs at different redshifts. Typically, LAEs have $f_{\rm esc}^{\rm Ly\alpha} \approx$ 20%–30% (Blanc et al. 2011; Nakajima et al. 2012; Song et al. 2014; Trainor et al. 2015; Matthee et al. 2021), while the average $f_{\rm esc}^{\rm Ly\alpha}$ in typical SFGs at $z \approx 2$–3 is less than 10% (Hayes et al. 2010; Kornei et al. 2010; Matthee et al. 2016; Sobral et al. 2017; Weiss et al. 2021; Reddy et al. 2022). This difference in the typical $f_{\rm esc}^{\rm Ly\alpha}$ between LAEs and SFGs indicates a possible correlation between Lyα escape and galaxy properties.

Theoretical and observational studies suggest that star formation in a compact region aids the escape of Lyα (and ionizing) photons (see Gnedin et al. 2008; Razoumov & Sommer-Larsen 2010; Heckman et al. 2011; Borthakur et al. 2014; Izotov et al. 2016; Ma et al. 2016; Reddy et al. 2016; Sharma et al. 2016; Kimm et al. 2019; Marchi et al. 2019; Ma et al. 2020; Naidu et al. 2020; Kakiichi & Gronke 2021; Reddy et al. 2022). The radiative, thermal, and mechanical feedback associated with the compactness of star formation can result in strong gas outflows. These outflows, in turn, can lead to "holes" or low column density channels in the ISM, thereby creating pathways for Lyα photons to escape. This physical mechanism is supported by several studies that suggest a correlation between star formation rate (SFR) surface density ($\Sigma_{\rm SFR}$) and Lyα escape (Heckman et al. 2011; Ma et al. 2016; Sharma et al. 2016; Verhamme et al. 2017; Marchi et al. 2019; Cen 2020; Naidu et al. 2020). Marchi et al. (2019) provided further evidence of this scenario by studying the role of kinematics and neutral hydrogen column density on Lyα emission using LAEs in the VANDELS survey. They found that the amount of scattering of Lyα photons is smaller for galaxies with higher interstellar gas outflow velocities, proposing that Lyα escape is larger in galaxies with strong feedback. However, they observed no correlation between Lyα escape and SFR, suggesting that other factors may be responsible for modulating Lyα escape. More recently, the effect of gravitational potential was investigated by considering the specific SFR (sSFR) surface density, $\Sigma_{\rm sSFR}$, which is $\Sigma_{\rm SFR}$ normalized by stellar mass (Kim et al. 2020; Reddy et al. 2022). Reddy et al. (2022) performed a spectroscopic survey of SFGs and found that Lyα escape is more efficient in low-mass galaxies coupled with high $\Sigma_{\rm SFR}$.

Apart from these internal factors, the large-scale environment around the galaxy (within $\sim$10 kpc of the galaxy) may play a role in regulating the gas covering fraction. Interactions with close neighbors are known to lead to starbursts in galaxies (Luo et al. 2014; Knapen & Cisternas 2015; Stierwalt et al. 2015; Moreno et al. 2021), which may in turn lead to conditions that favor the formation of low column density channels in the ISM through which Lyα photons may escape. While some studies find that LAEs in protoclusters have higher observed Lyα luminosities compared to field LAEs (Dey et al. 2016; Shi et al. 2019, 2020; Huang et al. 2021), other studies find similar or suppressed Lyα emission in protocluster galaxies (Lemaux et al. 2018; Malavasi et al. 2021). The differences can be partly attributed to selection effects and variations in the Lyα escape measurements. However, studies that find enhanced Lyα in dense regions also observe enhanced star formation in these galaxies.

In this paper, we investigate the role of different galaxy properties, such as stellar masses, SFRs, sizes, $\Sigma_{\rm SFR}$, $\Sigma_{\rm sSFR}$, and local environment, on the escape of Lyα using a sample of 62 LAEs at $z \approx 2.65$ in the Boötes region of the NOAO Deep Wide-Field Survey (NDWFS; Jannuzi & Dey 1999). Twenty-seven of these LAEs have confirmed spectroscopic redshifts, which enables more robust inferences of the stellar populations. The ground-based imaging of the Lyα emission line comes from the Subaru telescope, whose large aperture and sensitive optics provide us with access to some of the faintest LAEs (down to $\approx$0.1 $L^{\star}_{\rm Ly\alpha}$) at this redshift. We further use imaging from the Hubble Space Telescope (HST) in seven subfields, which contributes multiwavelength data for the analysis and a higher spatial resolution to study the sizes of galaxies. Three of the HST fields are in comparatively dense regions, providing an opportunity to study LAEs in different environments. To understand how Lyα escape depends on different properties, we compare the LAEs to a sample of 136 SFGs at $2.6 \leqslant z \leqslant 3.8$ that have deep rest-frame far-UV spectra from the MOSFIRE Deep Evolution Field (MOSDEF) survey (Kriek et al. 2015; Topping et al. 2020a; Reddy et al. 2022).

The outline of this paper is as follows. Section 2 describes the data used in this paper. The selection of LAEs and their photometry is outlined in Section 3. The derivation of different galaxy properties, as well as the proxies used to estimate Lyα escape, are detailed in Section 4. We describe the dependence of Lyα escape on different properties in Section 5 and present the conclusions in Section 6. Throughout the paper, we assume a flat universe cosmology with $\Omega = 0.287$ and $H_0 = 69.3$ km s^{-1} Mpc^{-1} (Hinshaw et al. 2013). All wavelengths are presented in air, and all magnitudes are given in the AB system (Oke & Gunn 1983).

2. Observations and Data Reduction

Prescott et al. (2008) searched for LAEs in an $\approx$1 deg^2 region (Figure 1) around a $z \approx 2.656$ Lyα blob (LAB; discovered by Dey et al. 2005) in the Boötes field of the NDWFS (Jannuzi & Dey 1999). They used the intermediate-band IA445 filter ($\lambda_c =$ 4458 Å, $\Delta\lambda_{\rm IA445} =$ 201 Å) on the SuprimeCam/Subaru telescope (Miyazaki et al. 2002), which probes the Lyα emission line at redshifts of $2.55 \leqslant z \leqslant 2.75$ (see Figure 2). Combining these deep observations with the optical broadband imaging from NDWFS, they uncovered $\approx$ 2200 candidate LAEs. Follow-up spectroscopy was performed on a subset of these candidates using MMT/Hectospec, which is a 300-fiber multiobject spectrograph with a 1° field of view (Fabricant et al. 2005). Hong et al. (2014) developed an automated algorithm to detect emission lines and measure the redshifts of candidates. This led to 876 confirmed redshifts, of which 711 are in the aforementioned redshift range. This is the single largest spectroscopic sample of LAEs in such a narrow redshift range to date. Details of the photometric and spectroscopic data are described by Prescott et al. (2008) and Hong et al. (2014), respectively.

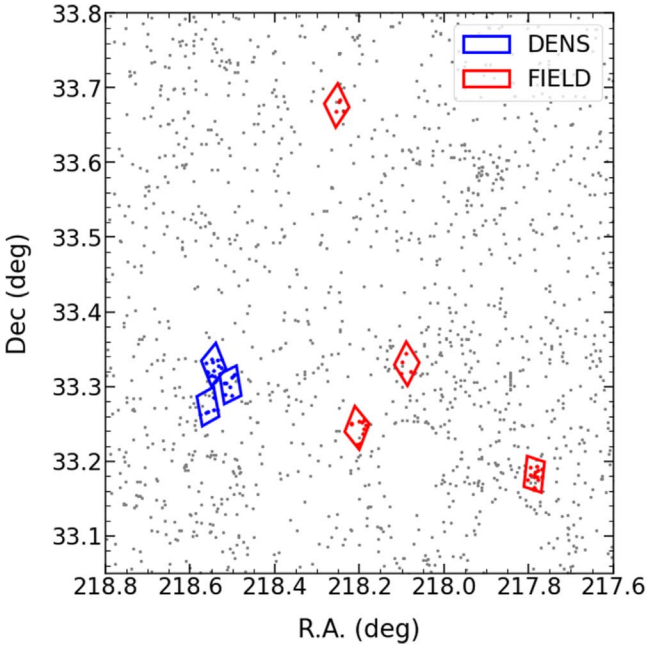

Figure 1. Overlap of the seven HST fields on the distribution of LAEs (shown in gray) from Prescott et al. (2008). The DENS and FIELD fields of view are shown in blue and red, respectively. The LAEs studied in this paper (see Section 3.2) are marked as blue and red points, depending on their HST fields.

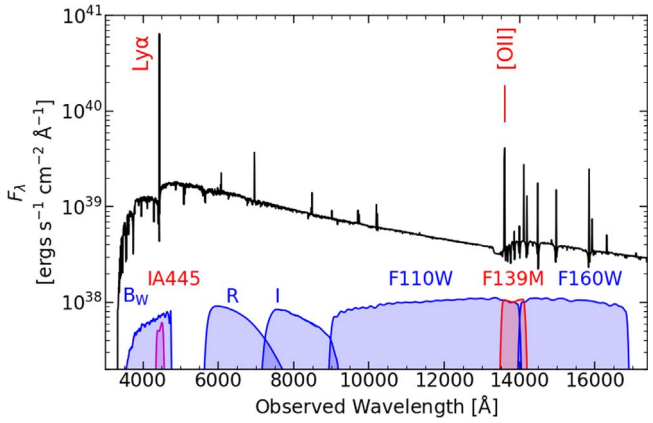

Figure 2. The SED of a model galaxy with age = 100 Myr, stellar metallicity, $Z_\star = 0.2\,Z_\odot$, and a constant star formation history. The model is generated using BAGPIPES (Carnall et al. 2018) and is redshifted to $z = 2.65$. Wavelengths corresponding to Lyα and [O II] emission lines at this redshift are marked. The broadband filters B_W, R, I, F110W, and F160W that are used in this analysis are shown from left to right in blue below. Similarly, the intermediate-band filters, IA445 and F139M, which probe the Lyα and [O II] lines, respectively, are shown in red.

Prescott et al. (2008) found that the number density of LAEs within $\approx$10′ of the LAB is almost three times higher than that of the LAEs in the field. Based on this local overdensity of LAE candidates, three high-density regions (DENS) within 3′ of the LAB and four low-density regions (FIELD) that are further away (>15′) were selected for studying LAEs in different environments. We obtained near-infrared images of these seven fields using the Wide-Field Camera 3 (WFC3; Dressel 2012) on the HST. The overlap of these fields on the entire $\approx$1 deg^2 field of view is shown in Figure 1. In this paper, we focus on the study of LAEs from these HST fields. The following subsection describes the HST observations and data reduction. In addition to the IA445 images, we include existing ground-based images in the following filters: B_W (λ_c = 4135 Å, $\Delta\lambda_{B_W}$ = 1278 Å); R (λ_c = 6514 Å, $\Delta\lambda_R$ = 1512 Å), and I (λ_c = 8205 Å, $\Delta\lambda_I$ = 1915 Å). The 5σ magnitude limits in 3″ diameter apertures in the B_W, IA445, R, and I bands are 26.4, 26.4, 25.6, and 25.1 mag, respectively.

2.1. HST Imaging

We obtained HST imaging of seven (three DENS and four FIELD) fields in the Boötes region during HST Cycle 20 (2013 April−November) as part of HST-GO-13000 (PI: S. Hong). Each field was observed in two broadband filters, F110W (λ_c = 11515 Å, $\Delta\lambda_{F110W}$ = 4996 Å) and F160W (λ_c = 15434 Å, $\Delta\lambda_{F160W}$ = 2875 Å), and a medium-band filter, F139M (λ_c = 13840 Å, $\Delta\lambda_{F160W}$ = 652 Å). The F139M filter covers the redshifted [O II] $\lambda\lambda$3726, 3729 at 2.5 $\lesssim z \lesssim$2.7 (Figure 2). The field of view of each of these fields is 123″ × 137″. Observations for each such pointing consisted of four orbits (F110W (one), F160W (one), and F139M (two)), and each orbit was observed with seven dithers. As a result, we obtained seven individual dithered images in F110W and F160W and 14 dithered images in F139M for every field.

We use AstroDrizzle (Avila et al. 2012) to align and drizzle all the individual images per filter per field onto a single frame. The output weight maps are effective exposure maps and reflect the relative weight of the individual pixels. These weight maps are used to create rms maps for the space-based images, which are needed to compute photometric uncertainties. We therefore astrometrically align both science and weight images to the IA445 images. For this purpose, we first use SExtractor (Bertin & Arnouts 1996) to identify stars on both sets of data (using DETECT_THRESH = 1.2 and CLASS_STAR $\geqslant$ 0.5). These stars are then used to align all the HST science and weight images to the ground-based images using the IRAF packages *ccmap* and *ccsetwcs* (Tody 1993). We also generate flag maps for the drizzled images from the weight maps as a measure of the data quality of the pixels. In order to perform multiband photometry, we register all the ground-based images, including the weight, rms, and flag maps, to the individual F110W science images in each field using the IRAF task *wregister*. The pixels where no HST data are available are set to zero for all the ground-based images. In summary, we have seven fields observed in seven different bands (B_W, IA445, R, I, F110W, F139M, and F160W). Each band has an associated science, exposure, rms, and flag image. The 5σ magnitude limits in 1″ diameter apertures in the F110W, F139M, and F160W bands are 26.9, 25.6, and 26.4 mag, respectively.

In Figure 2, we show the spectral energy distribution (SED) of a young model galaxy redshifted to $z = 2.65$, along with the response curves of all the filters used here. The seven filters together cover the rest-frame ultraviolet and optical region. Specifically, the broadband filters B_W, R, and I probe the rest-frame UV continuum of the galaxy; the F110W and F160W filters probe the Balmer break region of the SED; and the medium-band filters, IA445 and F139M, are positioned over the Lyα and [O II] emission lines, respectively.

2.2. Comparison Sample of High-redshift SFGs

To evaluate the properties of LAEs relative to typical galaxies at comparable redshifts, we select a sample of high-redshift galaxies from the MOSDEF survey (Kriek et al. 2015). The survey consists of rest-frame optical spectroscopy of $\approx$1500 *H*-band selected galaxies using the MOSFIRE

spectrograph (McLean et al. 2012) on the Keck I telescope. The SFGs were selected in three redshift ranges, $z = 1.37$–1.70, 2.09–2.61, and 2.95–3.80, in the CANDELS fields (Grogin et al. 2011; Koekemoer et al. 2011). The *H*-band limiting magnitudes of 24.0, 24.5, and 25.0 mag, respectively, for these redshift intervals ensure a roughly consistent stellar mass limit of $\sim 10^9\ M_\odot$ across all redshifts. Our comparison sample is a subset of these sources and consists of 136 typical SFGs that have complementary rest-frame far-UV spectra from the Low-Resolution Imaging Spectrometer (LRIS; Oke et al. 1995) on the Keck telescope. Details regarding this sample can be found in Topping et al. (2020a) and Reddy et al. (2022).

3. LAE Selection and Photometry

3.1. Source Detection and Photometry

We use the source detection algorithm, SExtractor, in dual-image mode for detecting sources and measuring their photometry (Bertin & Arnouts 1996). For this purpose, we combine the IA445 and B_W images in each field to construct a detection image. Individual images in every band are then taken as measurement images to calculate source fluxes. The parameters include DETECT_THRESH = 5.0, ANALYSIS_THRESH = 5.0, and DETECT_MINAREA = 10 pixels. We perform aperture photometry (FLUX_APER) in 12 different apertures with diameters ranging from $0\farcs25$ to $5''$. However, the photometric uncertainties produced by SExtractor are lower than the rms scatter in the images, suggesting that they are underestimated (FLUXERR_APER). To overcome this problem, we use the detected source positions to perform photometry using the python *photutils* package (Bradley et al. 2019). We compute the corresponding photometric uncertainties using the *calc_total_error* function that combines the background error with the Poisson noise of the sources, which is then compared to the rms scatter within each image. For every aperture, we consider the rms scatter as a lower limit for the flux error in that band. Based on the curve of growth and visual inspection of sources and the apertures, we use $3''$ diameter apertures for ground-based images. For each source in the HST images, we use either a $0\farcs75$ or $1''$ diameter aperture, selecting the one that yields a higher signal-to-noise ratio (S/N).

3.2. Selection of LAE Candidates

The Lyα emission line falls under the intermediate-band filter IA445 at the redshifts of interest (Figure 2). As a result, candidate LAEs will have excess emission in this band compared to the broadband, B_W. To identify LAE candidates, we compare the IA445 magnitude to the B_W magnitude. Even though this selection process of LAEs has been previously performed across the entire 1 deg^2 region (Prescott et al. 2008), we repeat the process on the seven HST fields.

We begin with all the sources that have IA445 and B_W magnitudes in the range 20 mag $\leqslant$ (B_W and IA445) $\leqslant$ 30 mag and the SExtractor output FLAGS $\leqslant 3$. This ensures that our sample is clean from objects that are near the image boundaries and/or have saturated pixels. We calculate the rms scatter in (IA445 − B_W) for different bins of IA445, and using these values, we obtain the rms scatter, $\sigma_{(\mathrm{IA445}-B_W)}$, as a function of IA445 magnitude. If there is no Lyα emission, the difference between IA445 and B_W depends on the UV slope of the galaxy SED, and we consider the median value of the difference of all the sources, $\overline{m}_{(\mathrm{IA445}-B_W)}$. We select LAE candidates based on the following conditions:

$$22 \leqslant \mathrm{IA445} \leqslant 28$$
$$\mathrm{S/N(IA445)} \geqslant 5$$
$$\mathrm{S/N(IA445} - B_W) \geqslant 5$$
$$(\mathrm{IA445} - B_W) \leqslant \overline{m}_{(\mathrm{IA445}-B_W)} - 1.5\sigma_{(\mathrm{IA445}-B_W)},$$

similar to the criterion used in Hao et al. (2018). In Figure 3, we show the color–magnitude diagram between (IA445 − B_W) and IA445 that was used for the selection of LAE candidates.

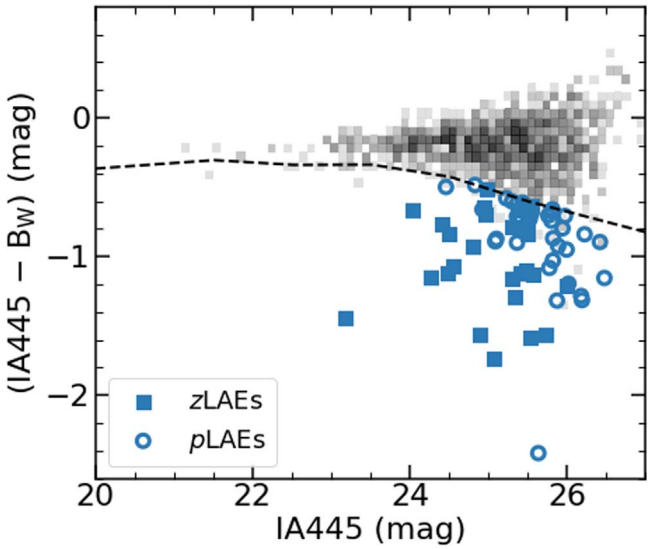

Figure 3. Color–magnitude diagram ((IA445 − B_W) vs. IA445) of all detected sources from the seven HST fields is shown by the 2D gray-scale histogram. The black dashed line denotes the criterion used for the selection of LAE candidates. The LAEs with confirmed spectroscopic redshifts in the range $2.55 \leqslant z \leqslant 2.75$ are shown as filled blue squares (*z*LAEs), while the photometric candidates are shown as open blue circles (*p*LAEs).

The selected LAEs may be contaminated by low-redshift [O II] emitters, where the [O II] emission line falls in the IA445 filter ($0.16 \leqslant z \leqslant 0.24$). Most of these are removed from the sample by applying a cut of (B_W − R) $\leqslant 0.7$ (see Figure 2 in Prescott et al. 2008). After removing these contaminants from our selection, we obtain a total of 74 possible candidates. We remove 10 sources based on visual inspection in both ground- and space-based images. Two of them are bright and spatially extended in the rest-frame optical regime and are likely low-redshift contaminants. There is a possibility that they might be true and unusually luminous high-redshift candidates, but we make a conservative decision to remove them from the sample. The remaining eight sources have artifacts in the images, like contamination from nearby sources, or they are located near WFC3/IR artifacts ("blobs") in the HST images (Pirzkal et al. 2010; Sunnquist 2018). After removing these objects, we are left with 64 LAE candidates overlapping the HST fields.

Twenty-nine of these candidates were observed spectroscopically (Hong et al. 2014) and are available in our LAE redshift catalog (Section 2). Of these, 26 sources have confirmed redshifts in the range $2.55 \leqslant z \leqslant 2.75$. From visual inspection of the spectra of the other three sources, we find faint Lyα emission in one of them (DENS3_118) that is missed by the automated redshift finding algorithm. We manually find the redshift of this source by fitting a Gaussian to the emission line. The remaining two spectra do not show any clear emission

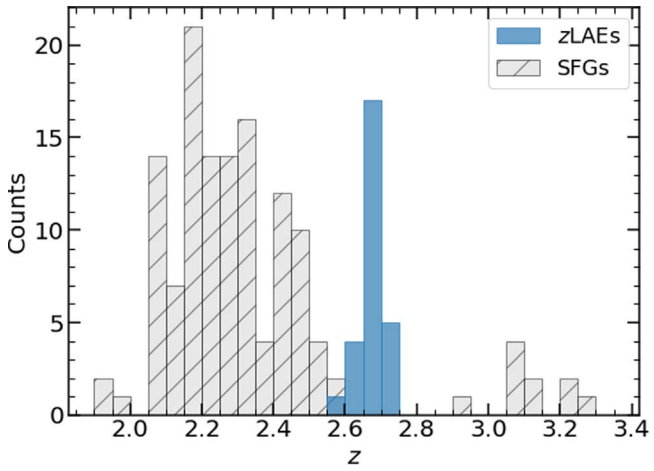

Figure 4. Redshift distribution of *z*LAEs and the comparison SFGs studied in this paper. The *z*LAEs are shown in filled blue, while the SFGs are shown in hatched gray. The median redshift of the *z*LAEs is ≈2.66, whereas we assume $z = 2.65$ for the *p*LAEs.

line in the wavelength region of interest, and their IA445photometry may be affected by skyline residuals. We remove these two sources from our catalog.

The final sample consists of 27 sources with confirmed spectroscopic redshifts, and we refer to these galaxies as *z*LAEs throughout this paper. The median redshift of these *z*LAEs is ≈2.66. We assume $z = 2.65$ for the rest of the 35 photometric LAE candidates (*p*LAEs), as this is the median redshift at which the IA445 band covers the Lyα emission line. From Figure 3, we find that the *p*LAEs have smaller (IA445 – B_W) excesses and appear to be fainter in the IA445 than the *z*LAEs. In Figure 4, we show the distribution of redshifts of *z*LAEs and SFGs (Section 2.2).

3.3. Photometric Measurements for SED Fitting

From a visual inspection of the LAEs, we find spatial offsets between Lyα emission and the stellar continuum, as has been observed in other LAE samples (Jiang et al. 2013; Hoag et al. 2019; Lemaux et al. 2021). Since the near-IR emission observed from HST is dominated by stellar continuum light, whereas the intermediate-band emission is dominated by Lyα emitted along the line of sight, the spatial distributions of the two are strongly affected by the relative distributions of gas, dust, and ionizing sources. In order to measure accurate photometry, we refit the LAE centers using the HST images. We estimate the source centroids by fitting a 2D Gaussian profile to the light distribution of each source in a $5'' \times 5''$ cutout. This new center does not affect the photometry of ground-based images because of the larger $3''$ aperture used, compared with the $0\farcs75$ (or $1''$) diameter used for the HST photometry.

We repeat the photometry of all the LAEs (27 *z*LAEs and 35 *p*LAEs) using these new centers. Due to the different sensitivity limits of the space- and ground-based data, the vastly different point-spread function (PSF) sizes, and the varying morphology as a function of wavelength, we choose to measure aperture photometry and select aperture sizes that optimize the S/N. The fluxes and corresponding uncertainties are computed using the python *photutils* package, as mentioned in Section 3.1. The coordinates, redshifts, and photometry of the final sample of 62 LAEs are presented in the Appendix.

4. Properties of LAEs

4.1. Emission-line Measurements

In this subsection, we describe the method used to measure the equivalent widths and fluxes of both Lyα and [O II] emission lines for all the LAEs. We use photometry from B_W, IA445, R, I, and F110W for Lyα emission-line measurements. We convert the magnitudes from these bands to flux densities (f_λ). We then fit a power law to these flux densities to calculate the continuum flux density at the central wavelength of the IA445 filter. We exclude IA445 flux density in this fit, given that it is contaminated by the Lyα emission. We repeat this process 10,000 times by varying each of the photometric measurements within its 1σ uncertainties. Since B_W does not probe the continuum alone, we use an error bar of $\pm 2\sigma$ for this band. The outputs of the repeated fits closely follow a normal distribution. Thus, the final continuum flux density probed by the IA445 filter ($f_{\lambda c;\mathrm{IA445}}$) and its error ($\delta f_{\lambda c;\mathrm{IA445}}$) are taken as the mean and standard deviation of the flux densities calculated from the repeated fits.

We calculate the Lyα flux and equivalent width using these continuum flux density measurements. Given the flux density ($f_{\lambda;\mathrm{IA445}}$) and its error ($\delta f_{\lambda;\mathrm{IA445}}$) measured from the IA445 magnitude, the Lyα flux ($F_{\mathrm{Ly}\alpha}$) and its error ($\delta F_{\mathrm{Ly}\alpha}$) are

$$F_{\mathrm{Ly}\alpha} = (f_{\lambda;\mathrm{IA445}} - f_{\lambda c;\mathrm{IA445}}) \times \Delta\lambda_{\mathrm{IA445}}, \quad (1)$$

$$\delta F_{\mathrm{Ly}\alpha} = \sqrt{(\delta f^2_{\lambda;\mathrm{IA445}}) + (\delta f^2_{\lambda c;\mathrm{IA445}})} \times \Delta\lambda_{\mathrm{IA445}}, \quad (2)$$

where $\Delta\lambda_{\mathrm{IA445}}$ is the FWHM of the IA445 filter. Furthermore, we calculate the rest-frame Lyα equivalent width ($W_{\mathrm{Ly}\alpha}$) and its error ($\delta W_{\mathrm{Ly}\alpha}$) as

$$W_{\mathrm{Ly}\alpha} = \frac{(f_{\lambda;\mathrm{IA445}} - f_{\lambda c;\mathrm{IA445}})}{f_{\lambda c;\mathrm{IA445}}} \times \frac{\Delta\lambda_{\mathrm{IA445}}}{(1+z)}, \quad (3)$$

$$\delta W_{\mathrm{Ly}\alpha} = \frac{f_{\lambda;\mathrm{IA445}}}{f_{\lambda c;\mathrm{IA445}}} \times \sqrt{\left(\frac{\delta f_{\lambda;\mathrm{IA445}}}{f_{\lambda;\mathrm{IA445}}}\right)^2 + \left(\frac{\delta f_{\lambda c;\mathrm{IA445}}}{f_{\lambda c;\mathrm{IA445}}}\right)^2} \times \frac{\Delta\lambda_{\mathrm{IA445}}}{(1+z)}. \quad (4)$$

We are not accounting for the correction due to the Lyman forest here, due to which we slightly underestimate the Lyα measurements. This estimated flux is used to correct B_W for emission, as described in Section 4.1.1.

Similarly, we calculate the [O II] flux ($F_{[\mathrm{O\,II}]}$) and equivalent width ($W_{[\mathrm{O\,II}]}$) by considering the photometry from the F110W, F139M, and F160W bands. By varying the flux densities from the F110W and F160W bands within their uncertainties, we fit a power law to calculate the continuum flux density at the central wavelength of the F139M filter. The [O II] flux and equivalent width, along with their errors, are

$$F_{[\mathrm{O\,II}]} = (f_{\lambda;\mathrm{F139M}} - f_{\lambda c;\mathrm{F139M}}) \times \Delta\lambda_{\mathrm{F139M}}, \quad (5)$$

$$\delta F_{[\mathrm{O\,II}]} = \sqrt{(\delta f^2_{\lambda;\mathrm{F139M}}) + (\delta f^2_{\lambda c;\mathrm{F139M}})} \times \Delta\lambda_{\mathrm{F139M}}, \quad (6)$$

$$W_{[\mathrm{O\,II}]} = \frac{(f_{\lambda;\mathrm{F139M}} - f_{\lambda c;\mathrm{F139M}})}{f_{\lambda c;\mathrm{F139M}}} \times \frac{\Delta\lambda_{\mathrm{F139M}}}{(1+z)}, \quad (7)$$

$$\delta W_{[\mathrm{O\,II}]} = \frac{f_{\lambda;\mathrm{F139M}}}{f_{\lambda c;\mathrm{F139M}}} \times \sqrt{\left(\frac{\delta f_{\lambda;\mathrm{F139M}}}{f_{\lambda;\mathrm{F139M}}}\right)^2 + \left(\frac{\delta f_{\lambda c;\mathrm{F139M}}}{f_{\lambda c;\mathrm{F139M}}}\right)^2} \times \frac{\Delta\lambda_{\mathrm{F139M}}}{(1+z)}, \quad (8)$$

where $f_{\lambda;\mathrm{F139M}}$ and $\delta f_{\lambda;\mathrm{F139M}}$ are the flux density and its error measured from the F139M filter, $f_{\lambda c;\mathrm{F139M}}$ and $\delta f_{\lambda c;\mathrm{F139M}}$ are the continuum flux density and its error computed from the rest-frame optical continuum fitting, and $\Delta\lambda_{\mathrm{F139M}}$ is the FWHM of the F139M filter. For the LAEs where there is no clear [O II] emission from F139M, i.e., when the flux densities measured by F139M are less than the continuum expected at this filter, we place 3σ upper limits on both the flux and equivalent width measurements.

The Lyα equivalent width and flux measurements for the SFGs are computed using the rest-frame far-UV LRIS spectra (Reddy et al. 2022), while their [O II] flux measurements are obtained from the rest-frame optical spectra from MOSFIRE (Kriek et al. 2015; Reddy et al. 2018a) of the galaxies. The LRIS and MOSFIRE spectra are corrected for slit loss, so the fluxes and equivalent widths derived should be similar to those obtained from photometry and can be used for the purposes of our comparison.

4.1.1. Correcting $\mathrm{B_W}$ for Lyα Flux

In order to fit the stellar continuum using the measured photometry, we first need to correct the broadband filter for contamination from nebular emission lines. For the $z \approx 2.65$ LAEs, the $\mathrm{B_W}$ filter bandpass samples the Lyα emission line, the UV continuum emission, and the Lyman forest absorption. The $\mathrm{B_W}$ flux is corrected for Lyα emission as described below.

Using the flux density and its error from the $\mathrm{B_W}$ filter ($f_{\lambda;\mathrm{B_W}}$ and $\delta f_{\lambda;\mathrm{B_W}}$), we calculate the flux from the filter, $F_{\mathrm{B_W}}$, and its error, $\delta F_{\mathrm{B_W}}$,

$$F_{\mathrm{B_W}} = f_{\lambda;\mathrm{B_W}} \times \Delta\lambda_{\mathrm{B_W}}, \quad (9)$$

$$\delta F_{\mathrm{B_W}} = \delta f_{\lambda;\mathrm{B_W}} \times \Delta\lambda_{\mathrm{B_W}}, \quad (10)$$

where $\Delta\lambda_{\mathrm{B_W}}$ is the FWHM of the $\mathrm{B_W}$ filter. The corrected flux density and its error in the $\mathrm{B_W}$ filter ($f_{\lambda\mathrm{corr};\mathrm{B_W}}$ and $\delta f_{\lambda\mathrm{corr};\mathrm{B_W}}$) are then

$$f_{\lambda\mathrm{corr};\mathrm{B_W}} = \frac{(F_{\mathrm{B_W}} - F_{\mathrm{Ly}\alpha})}{\Delta\lambda_{\mathrm{B_W}}}, \quad (11)$$

$$\delta f_{\lambda\mathrm{corr};\mathrm{B_W}} = \frac{\sqrt{(\delta F^2_{\mathrm{B_W}}) + (\delta F^2_{\mathrm{Ly}\alpha})}}{\Delta\lambda_{\mathrm{B_W}}}. \quad (12)$$

This corrected flux density and its error are converted back to the magnitude system, which are then used as proper continuum measurements of the LAEs at the central wavelength of the $\mathrm{B_W}$ filter. While these estimates for the corrections to the $\mathrm{B_W}$ photometry are simplistic, more sophisticated approaches will not significantly change the results given the photometric uncertainties of these faint LAEs.

For one particular LAE, FIELD2_149, the Lyα flux is high compared to the $\mathrm{B_W}$ flux due to a nondetection in the continuum (S/N in $\mathrm{B_W} \sim 0.6$). As a result, correcting the $\mathrm{B_W}$ results in a negative value. Given this nonphysical flux value, we use the $\mathrm{B_W}$ magnitude as it is but with 2σ error bars when fitting the SED. This ensures a larger range for the $\mathrm{B_W}$ fluxes to vary while decreasing the weight relative to other bands.

4.2. SED Fitting

We fit the SED of the LAEs using the Bruzual & Charlot (2003) stellar population models. We correct the broad $\mathrm{B_W}$ filter for the Lyα contribution (Section 4.1.1) and do not use IA445 or F139M photometry for the SED fitting. We assume a Salpeter initial mass function (IMF; Salpeter 1955) and a constant star formation history. We consider a stellar metallicity of $Z_\star = 0.28\,Z_\odot$, as subsolar metallicity models provide a better fit to the photospheric line blanketing that is observed in the rest-frame UV spectra of typical SFGs at $z \gtrsim 2$ (Steidel et al. 2016; Cullen et al. 2020; Topping et al. 2020b, 2020a; Kashino et al. 2022; Reddy et al. 2022). We also assume an SMC extinction curve (Gordon et al. 2003), as motivated in other studies of high-redshift SFGs (Reddy et al. 2018b; Shivaei et al. 2020). The reddening values are allowed to vary in the range $0 \leqslant E(B-V) \leqslant 0.6$. We note that changing the star formation history to exponentially increasing or varying the stellar metallicity does not significantly affect our results. We allow the ages to vary from 10 Myr to the age of the universe at the redshift of each galaxy. When fitting for stellar populations, we use the spectroscopic redshifts for the zLAEs, while we set $z = 2.65$ for the pLAEs. The best fit is selected as the one with the minimum χ^2 with respect to the photometry. We refit the best-fit model multiple times by perturbing the photometry within the uncertainties and recomputing the parameter values each time. In most cases where the parameters do not reach the edge of the SED grid, the estimated parameters from the perturbed data are normally distributed. The uncertainties in these parameters are then taken as the standard deviation of these different measurements. More details about the fitting procedure are described by Reddy et al. (2015).

From the SED fitting, we obtain estimates of stellar masses ($M_\star$), ages, SFRs, and dust reddening of the individual LAEs. We also consider the properties of SFGs (Section 2.2) using the same SED fitting procedure (Reddy et al. 2015). Age is the least constrained parameter and should be considered with caution.

Figure 5 shows three examples of SED fits, along with $5'' \times 5''$ image cutouts of the LAEs in different bands. The flux densities shown as red circles probe the Lyα and [O II]emission lines at the LAE redshift and are not used for the SED fitting. The top panel shows an example of an LAE, which has a noticeable emission in all seven bands, including faint emission in R and I. In this case, the SED model provides a reasonable fit to the photometry. In the middle panel, we show a case where the LAE is not visible in R and I. The resulting fit depends on $\mathrm{B_W}$, F110W, and F160W photometry. Most of the sources in our sample have such comparable data. Due to the faintness of the galaxy in the bottom panel, it is only observable in the IA445 band that probes the Lyα emission line. The faint photometry of this LAE in all the other filters results in an uncertain SED fit. Nine LAEs in our sample ($\approx$14%) have such uncertain fits. Photometric uncertainties are taken into account in the fitting procedure and our physical interpretation of the results.

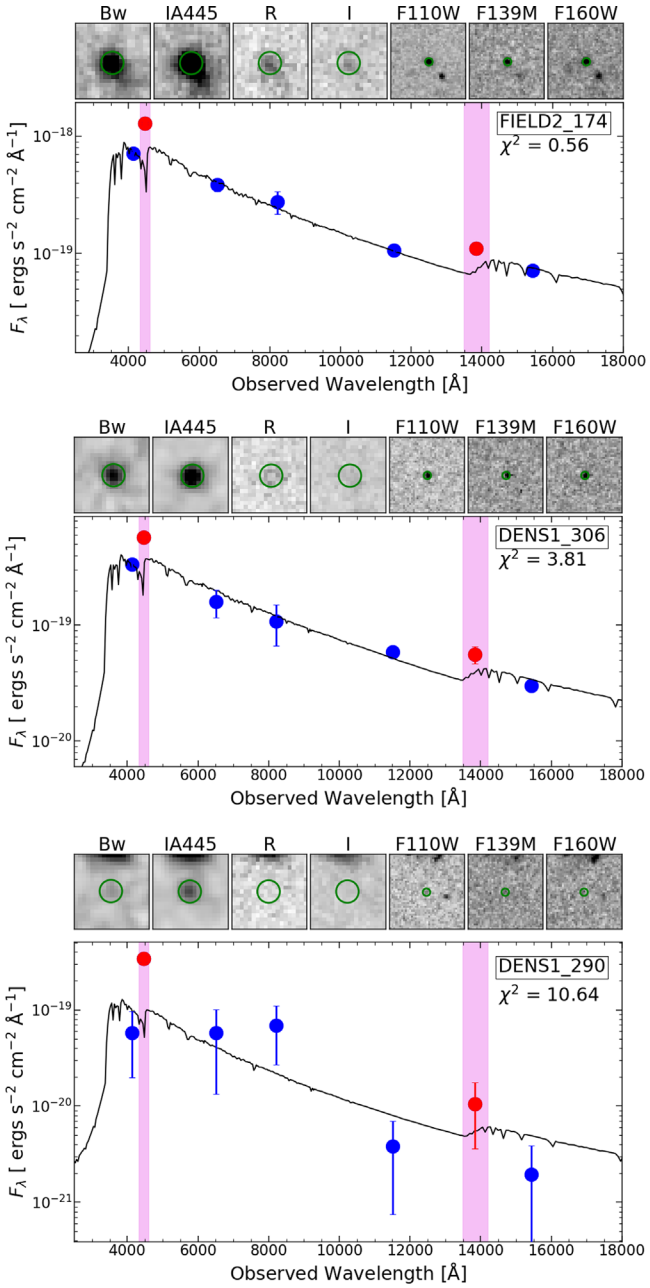

Figure 5. Example SEDs with their best-fit model. Image cutouts (5″ × 5″) of the LAEs in different bands (B_W, IA445, R, I, F110W, F139M, and F160W from left to right) are shown at the top of each panel for each LAE. The green circles on the images are the apertures used for performing photometry. The top, middle, and bottom panels show examples of good, acceptable, and uncertain SED fits, respectively. The blue circles in each panel are flux densities in the B_W (corrected for Lyα flux), R, I, F110W, and F160W bands (from left to right in each panel) that are used for the SED fitting. The minimum χ^2 best-fit SED is overplotted, with the χ^2 value shown on the plot. The red points show the IA445 and F139M flux densities, which probe the Lyα and [O II] emission lines, respectively. The pink shaded regions mark the wavelength range of these filter passbands.

4.2.1. Stellar Populations of LAEs

Figure 6 shows the distribution of properties of LAEs and SFGs derived from SED fitting. The median values for the individual parameters for both samples are shown as dashed vertical lines. In Table 1, we show the quartile values of these parameters for *z*LAEs, *p*LAEs, all LAEs together, and SFGs.

We find that the sample of LAEs (both *z*LAEs and *p*LAEs) contains young populations. The minimum age of the sample is restricted to be 10 Myr via SED fitting. However, it is possible that the galaxies with this borderline age from SED fitting might have ages less than 10 Myr. These are most likely compact galaxies with short dynamical timescales (see Section 4.3). All LAEs are found to be younger than 1 Gyr, with a median of ≈20 Myr. Given the typical uncertainties (≳40 Myr) in this parameter, any interpretations regarding the age should be carefully considered. The LAEs also have low dust reddening values, 0 mag $\leqslant E(B-V) \leqslant$ 0.26 mag, with a median of 0.08 mag. The *p*LAEs are, on average, older and have more dust content than the *z*LAEs (Table 1).

The LAEs have stellar masses in the range 7.2 $\leqslant \log(M_\star/M_\odot) \leqslant$ 9.6, with a median of $\log(M_\star/M_\odot) \approx 8.6$. The SFRs measured for the LAEs range from ≈0.8 to ≈100 $M_\odot$ yr^{-1}, with a median of ≈10 $M_\odot$ yr^{-1}. These are in agreement with the measurements of stellar masses and SFRs in typical LAEs detected using narrowband techniques at z ∼2–3 (Nilsson et al. 2011; Vargas et al. 2014; Sandberg et al. 2015; Shimakawa et al. 2017; Hao et al. 2018; Kusakabe et al. 2018). We also find that the *p*LAEs are, on average, more massive and have higher SFRs compared to *z*LAEs.

Table 1 shows the Kolmogorov–Smirnov (K-S) test results between the *z*LAEs and *p*LAEs for the different parameters. Even though both samples are selected using the same criterion, the *p*-values for stellar mass and SFR, in particular, suggest that the two distributions may not share the same parent sample. The LAEs with fainter (or less luminous) Lyα emission tend to be redder and more massive, similar to what we have observed (e.g., Pentericci et al. 2009; Finkelstein et al. 2011; Hathi et al. 2016; Du et al. 2018, 2021; Reddy et al. 2022). Additionally, the *p*LAEs might have a possible low-redshift contamination, and the lack of spectroscopic redshifts introduces higher uncertainties in the SED fitting results.

On comparing the LAEs with the SFGs, we find that the LAEs are younger and have slightly lower dust content than the SFGs. In fact, the median age of the SFGs is ≈1 Gyr, which is closer to the upper limit of the age of the LAEs. Additionally, the LAEs are, on average, less massive and have similar SFRs compared to SFGs. The K-S test for all the parameters clearly suggests that the two samples have different underlying distributions (Table 1). We explore the locations of LAEs and SFGs on the star-forming main-sequence (SFMS) diagram below.

4.2.2. Star-forming Main Sequence

The position of typical SFGs in $M_\star$–SFR space follows a power law, often called the SFMS (Brinchmann et al. 2004; Daddi et al. 2007; Elbaz et al. 2007; Noeske et al. 2007). Some studies have found LAEs to lie above the SFMS (Hagen et al. 2014; Vargas et al. 2014; Hagen et al. 2016; Hao et al. 2018), while others have found LAEs on the SFMS (Shimakawa et al. 2017; Kusakabe et al. 2018). The SFMS evolves with redshift, and these comparisons should be made with galaxies at similar redshifts. The location of a galaxy on the SFMS can help us understand the "mode" of star formation happening within it. Galaxies that lie on the SFMS are considered to be "normal" SFGs, while galaxies undergoing a current burst of star formation tend to reside above this sequence. Understanding the location of LAEs relative to the main sequence can provide clues to the star formation history of the LAEs.

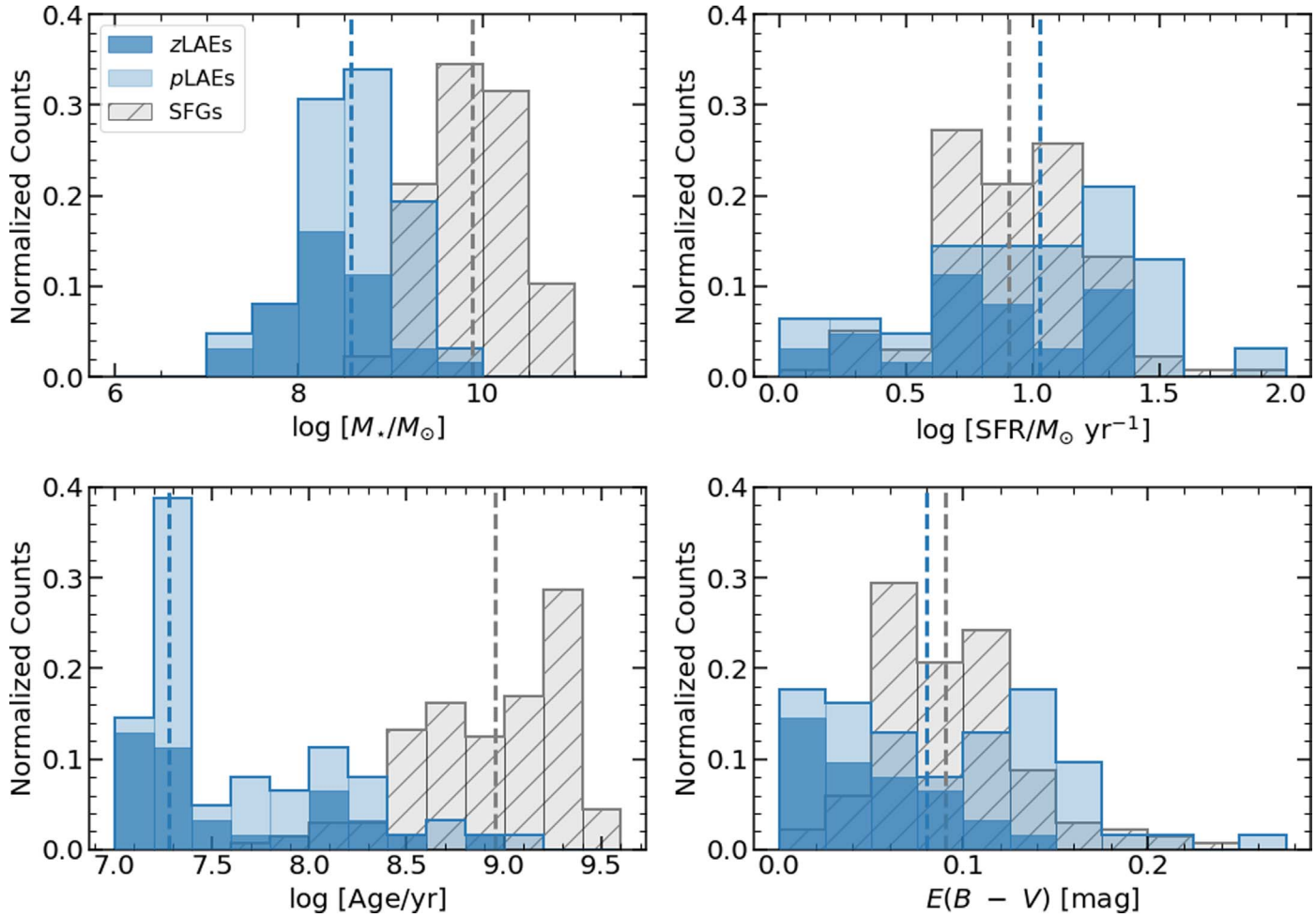

Figure 6. Distribution of stellar mass (top left), SFR (top right), age (bottom left), and dust reddening (bottom right) of the LAEs computed from the SED fitting. In each of the panels, the dark blue shaded bars are the *z*LAEs, while the light blue shaded bars are the *p*LAEs. The distributions of typical SFGs are overplotted in hatched gray. The median values of each parameter for the LAEs and SFGs are marked by dotted blue and gray vertical lines, respectively. The histograms in all the panels are normalized by the total number of sources.

Table 1
Median Values of Parameters for Different Sets of Galaxies

Galaxy Sample	Number of Sources	log $M_\star$ ($M_\odot$)	SFR ($M_\odot$ yr^{-1})	Age (Myr)	$E(B-V)$ (mag)
*z*LAEs	27	8.3 [8.0, 8.7]	5.4 [3.6, 13.0]	19 [15, 101]	0.04 [0.01, 0.075]
*p*LAEs	35	8.7 [8.5, 9.1]	15.5 [8.1, 25.8]	25 [19, 90]	0.13 [0.075, 0.155]
K-S test *p*-value	⋯	0.009	0.006	0.179	0.280
All LAEs	62	8.6 [8.3, 8.9]	10.6 [4.7, 20.3]	19 [19, 101]	0.08 [0.04, 0.13]
MOSDEF	136	9.9 [9.6, 10.2]	8.0 [6.0, 14.0]	910 [404, 1609]	0.09 [0.06, 0.11]
K-S test *p*-value	⋯	1.1×10^{-33}	0.019	2.4×10^{-34}	0.005

Note. The numbers in square brackets denote the 25th and 75th percentiles for each parameter.

Figure 7 shows the log [SFR/$M_\odot$ yr^{-1}] versus log [$M_\star/M_\odot$] plot for the LAEs and SFGs. Two other LAE samples from Hagen et al. (2016) at $z \sim 2$ (referred to as H16) and Shimakawa et al. (2017) at $z \sim 2.5$ (referred to as Sh17) are also plotted. The stellar masses and SFRs from Shimakawa et al. (2017) were computed from the SED fitting technique assuming a Chabrier IMF (Chabrier 2003). We multiply them by 1.897 in order to scale them to the Salpeter IMF for consistency with the other data shown in Figure 7. Parameterizations for the SFMS computed by Whitaker et al. (2014), Schreiber et al. (2015), and Shivaei et al. (2015) are overplotted and extended to lower masses ($M_\star \lesssim 10^{8.5} M_\odot$) in dotted, dashed, and solid lines, respectively. The artificial tight relation between the stellar mass and SFR, as demonstrated by blue points in the figure, is due to the young ages of the LAEs. Both SFR and $M_\star$ depend on the normalization of the best-fit SED to the photometry. As a result, these two parameters are tightly correlated, especially for a constant star formation history model.

We find that most of the LAEs lie above the SFMS relation, indicating an elevated SFR for their stellar mass. This suggests that most LAEs may be undergoing a bursty mode of star formation. In order to explore how much the LAEs deviate from the SFMS, we plot the separation of galaxies from the

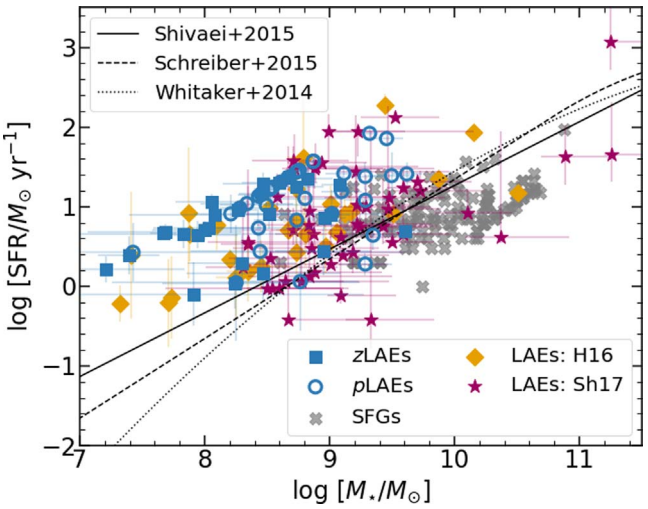

Figure 7. Position of LAEs relative to the SFMS on the log $M_\star$ vs. log SFR space. The samples of *z*LAEs and *p*LAEs are plotted as filled blue squares and open blue circles, respectively. The MOSDEF comparison SFGs are shown as gray crosses. Previous results of LAEs from Hagen et al. (2016; shown as H16) and Shimakawa et al. (2017; shown as Sh17) are displayed as orange diamonds and magenta stars, respectively. The main-sequence parameterizations computed by Whitaker et al. (2014), Schreiber et al. (2015), and Shivaei et al. (2015) are extended to lower masses and overplotted as dotted, dashed, and solid lines, respectively.

SFMS ($d_{\rm SFMS}$), parameterized by Shivaei et al. (2015), as a function of stellar mass in Figure 8. The horizontal dashed line denotes the expected values when a galaxy lies on the SFMS for a given $M_\star$. We are assuming that the SFMS parameterization extends to lower masses as well. Seventeen out of 62 (≈28%) LAEs lie within 2σ of the SFMS, but the majority of sources ($\gtrsim$70%) are well above the relation. Their star-forming modes range from "bursty" to "normal" star formation. For a given stellar mass, LAEs typically have a more starbursty nature compared to SFGs. However, the position of galaxies on the SFMS will also depend on their ages. The larger separations from the SFMS indicate that for a given stellar mass, LAEs tend to be younger than SFGs. More massive LAEs lie on the main sequence compared to their less massive counterparts (similar to Santos et al. 2020). However, it is possible that we are missing galaxies that have low masses as well as low SFRs. Continuum-based searches are magnitude-limited and tend to select higher-mass galaxies, while Lyα emission–based searches select galaxies with higher Lyα emission, which is mostly a result of higher SFRs.

The top and right panels of Figure 8 show normalized histograms of the stellar masses and $d_{\rm SFMS}$ of the different galaxy populations, respectively. The observed peak in $d_{\rm SFMS}$ is from the LAEs that border the artificial relation in Figure 7. Combining our results with those of LAEs in the literature, we observe that LAEs, on average, lie above the SFMS compared to typical SFGs. On the other hand, LAEs are, on average ≈1.5 dex less massive than SFGs. This indicates that galaxies selected via the Lyα emission line almost always probe the low-mass end of the galaxy mass function and have higher sSFRs, on average, compared to typical SFGs.

4.3. Morphology of LAEs

Previous studies have shown that LAEs are compact in the rest-frame UV and optical continuum (Bond et al. 2009; Gronwall et al. 2011; Bond et al. 2012; Malhotra et al. 2012; Paulino-Afonso et al. 2018; Shibuya et al. 2019). We compute the sizes of our sample of LAEs using the HST F110W images with the aim of estimating their SFR surface densities, as well as comparing them to typical SFGs. The sizes and SFR surface densities of the MOSDEF SFGs are presented in Reddy et al. (2022), and we will refer to that study for comparison.

4.3.1. Rest-frame Optical Size Measurements

To measure the sizes from HST images, we first compute the PSF of these images using GALFIT (Peng et al. 2010). We find stars by running SExtractor on all the F110W images based on the CLASS_STAR parameter. We then run GALFIT on these stars with a Sérsic 2D profile (Sérsic 1963) by fixing the Sérsic index, $n = 0.5$, which is identical to a 2D Gaussian profile. The resulting effective radius (r_e) is taken as the effective radius of the PSF. GALFIT fails to converge when trying to run with an input PSF, suggesting that the LAEs are barely resolved. To circumvent this, we estimate the LAE sizes by running GALFIT without an input PSF profile to the fitting tool. This results in sizes from the images that are not yet corrected for the PSF. We fix $n = 1$ to compute the effective radius of galaxies using a Sérsic 2D profile. Given the limiting PSF resolution, there is no obvious difference in the results when we vary the value of the Sérsic index. We correct the resulting radius for the PSF by subtracting the r_e of the PSF from it in quadrature. In order to check the validity of our sizes, we compute the r_e of all the LAEs using the F160W continuum images using the same method as above. The sizes derived from F110W and F160W images are consistent within the uncertainties.

We consider all sources that have r_e within 2σ of the PSF as unresolved sources, and we set the r_e of the PSF as the upper limit to their sizes. The left panel of Figure 9 shows the distribution of these sizes. We find that 37 out of 64 LAE candidates (≈60%) are unresolved ($r_e \lesssim 1$ kpc). If we consider the fraction of unresolved galaxies as a degree of compactness for a particular population of galaxies, then most studies of LAEs find a higher fraction of unresolved galaxies than LBGs or typical SFGs at a given stellar mass. The SFGs with stellar masses $\gtrsim 10^9\,M_\odot$ at $z \sim 2-3$ are more spatially extended, with sizes in the range of $r_e \sim$ 0.7–3 kpc (Law et al. 2012; Shibuya et al. 2015). Additionally, studies have found that LAEs are smaller than typical SFGs across all redshifts (Paulino-Afonso et al. 2018).

The LAEs have sizes that are independent of redshift (Malhotra et al. 2012; Kim et al. 2021). This is in contrast with the size evolution observed in SFGs and LBGs (Shibuya et al. 2015). This means that galaxies selected based on their strong Lyα emission are mostly compact in nature, suggesting that Lyα escape might be related to the sizes of galaxies (Section 5.2).

4.3.2. SFR Surface Densities

The distribution of star formation in galaxies may influence the escape of Lyα photons from them (Section 1). To probe this connection, we measure the SFR surface density, $\Sigma_{\rm SFR}$:

$$\Sigma_{\rm SFR}[M_\odot\ {\rm yr}^{-1}\,{\rm kpc}^{-2}] = \frac{\rm SFR}{2\pi r_e^2}. \quad (13)$$

In the middle panel of Figure 9, we show the distribution of $\Sigma_{\rm SFR}$ of our sample of LAEs. We find lower limits for the unresolved sources, which are shown as a dotted histogram in

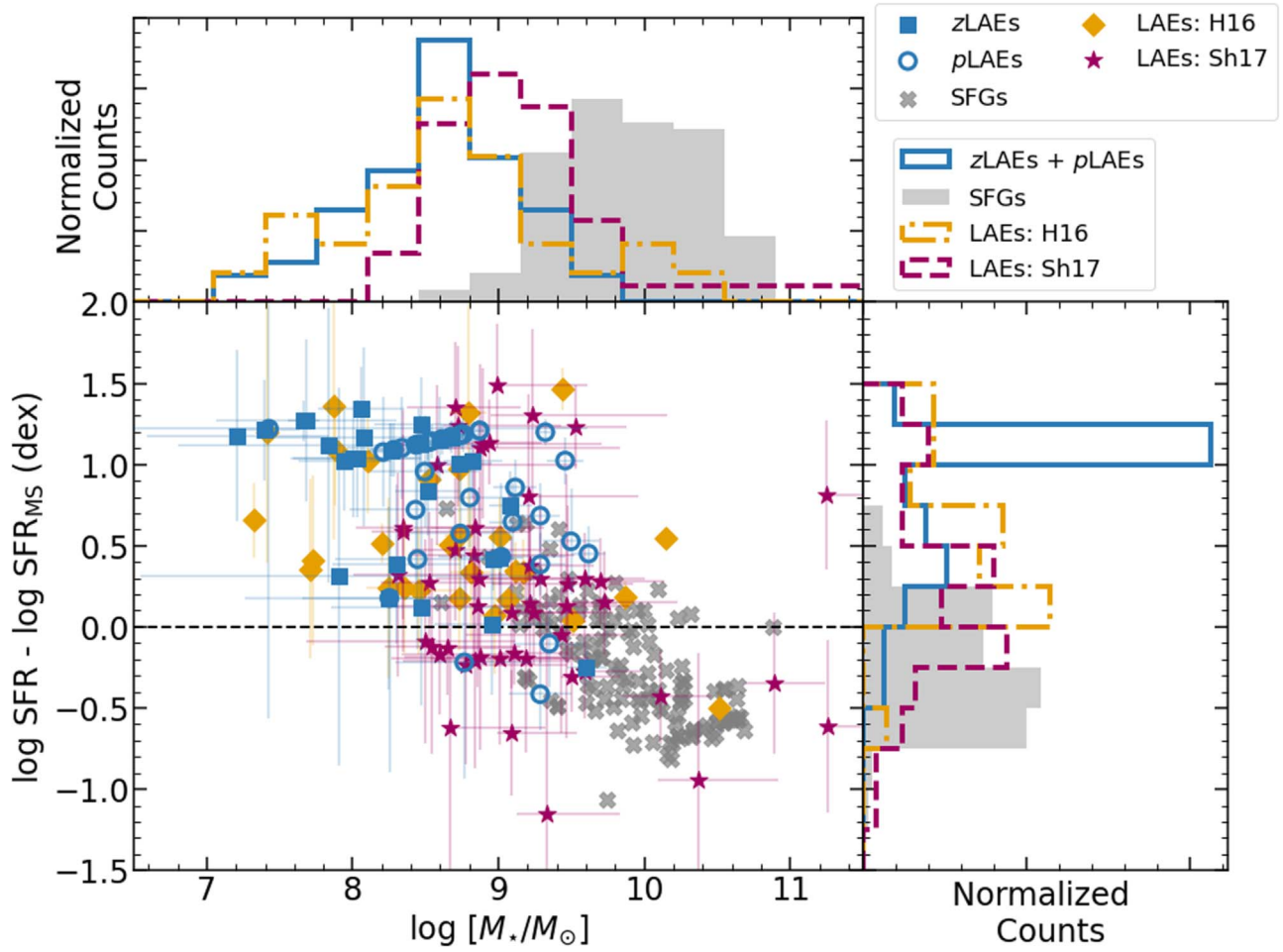

Figure 8. Main panel: separation (d_{SFMS}) of LAEs and SFGs from the SFMS parameterization by Shivaei et al. (2015) as a function of stellar mass. The colors and symbols are the same as in Figure 7. Top panel: histogram of stellar masses for the different samples of galaxies. Right panel: histogram of d_{SFMS} for the different samples of galaxies.

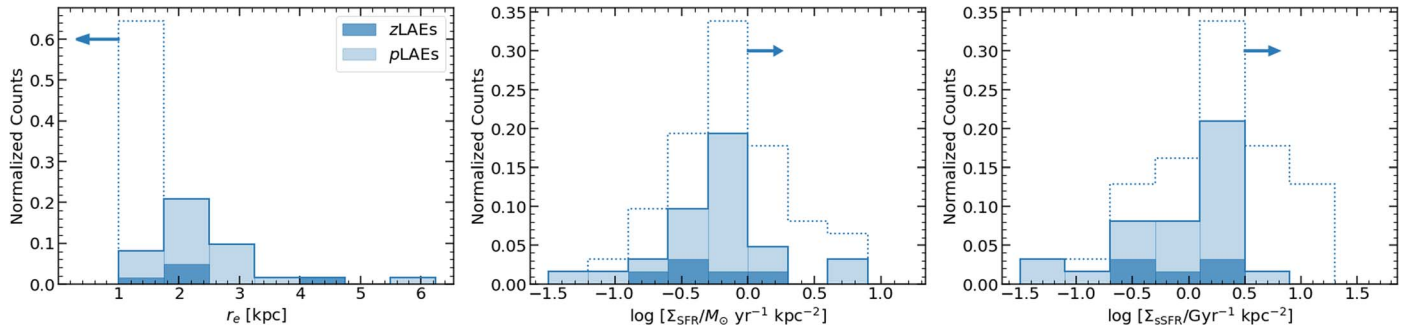

Figure 9. Distribution of sizes (r_e; left), SFR surface densities (Σ_{SFR}; middle), and sSFR surface densities (Σ_{sSFR}; right) of the LAEs. The colors are the same as in Figure 6. The upper limits on the sizes of the unresolved galaxies and the corresponding lower limits on the surface densities are shown as dotted histograms.

the figure. From resolved sources, we find that the LAEs have $\Sigma_{SFR} \gtrsim 1$–$100\,M_\odot\,yr^{-1}\,kpc^{-2}$. This is higher than the values for typical SFGs at $2 \lesssim z \lesssim 3$, which have $\Sigma_{SFR} \approx 10^{-2}$–$10\,M_\odot\,yr^{-1}\,kpc^{-2}$ (Shibuya et al. 2015; Reddy et al. 2022).

Previous studies suggest that the gravitational potential may also play a role in Lyα escape (Kim et al. 2021; Reddy et al. 2022). We consider stellar mass as a proxy for this potential (e.g., see Reddy et al. 2022, for more details) and compute the sSFR surface density, Σ_{sSFR}, to quantify this effect:

$$\Sigma_{sSFR}[Gyr^{-1}\,kpc^{-2}] = \frac{\Sigma_{SFR}}{M_\star}. \quad (14)$$

The distribution of Σ_{sSFR} is shown in the right panel of Figure 9, which includes lower limits for unresolved sources. The LAEs have $\Sigma_{sSFR} \gtrsim 0.03$–$10\,Gyr^{-1}\,kpc^{-2}$, while SFGs typically have $\Sigma_{sSFR} \approx 10^{-3}$–$10\,Gyr^{-1}\,kpc^{-2}$ (Reddy et al.2022).

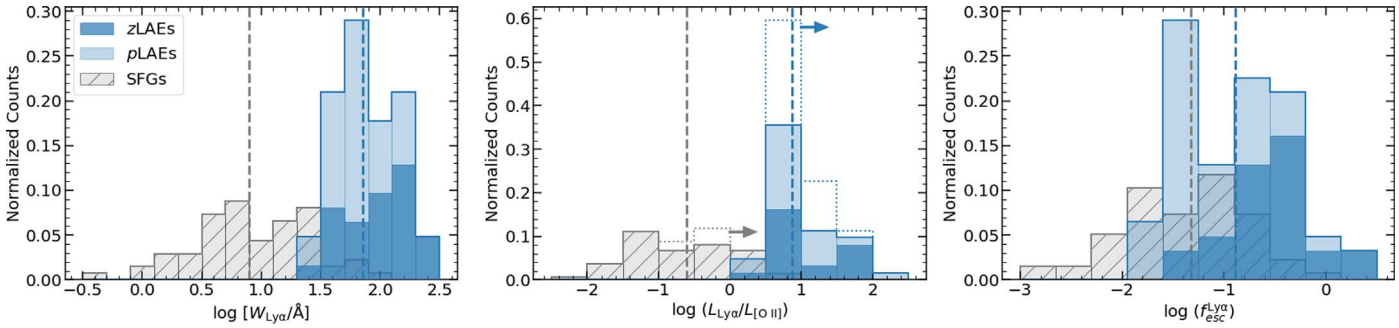

Figure 10. Three different measurements for studying the escape of Lyα in galaxies. Left: Lyα equivalent width, $W_{Ly\alpha}$. Middle: ratio of Lyα to [O II] luminosity. Right: escape fraction, $f_{esc}^{Ly\alpha}$. The colors are the same as in Figure 6. The median values for LAEs and SFGs are indicated by dashed blue and gray vertical lines, respectively.

4.4. Proxies for Lyα Escape

We quantify the escape of Lyα photons using three different measurements: the Lyα equivalent width ($W_{Ly\alpha}$), the ratio of Lyα to [O II] luminosity (Lyα/[O II]), and the escape fraction ($f_{esc}^{Ly\alpha}$). It is important to note that we are measuring the Lyα escape only along the line of sight and are not accounting for photons that are resonantly scattered into the diffuse halo. Even though these proxies are sensitive to the gas covering fraction and the dust content in galaxies, they are different measures of the observed Lyα emission.

The equivalent width of the Lyα emission ($W_{Ly\alpha}$) is the least model-dependent proxy for the Lyα escape (Sobral & Matthee 2019). The calculation of $W_{Ly\alpha}$ for LAEs and SFGs is described in Section 4.1. In the left panel of Figure 10, we show the distribution of $W_{Ly\alpha}$ for LAEs and SFGs. The LAEs have higher $W_{Ly\alpha}$ ranging from 20 to 250 Å with a median of ≈70 Å. In contrast, the SFGs with observable Lyα emission have a median $W_{Ly\alpha}$ of ≈7.8 Å. This difference is mostly by selection, since galaxies with high $W_{Ly\alpha}$ are likely to be selected via narrowband imaging and more likely to be spectroscopically confirmed.

The ratio of Lyα to [O II] luminosity is another possible proxy for the escape of Lyα, which depends on the distribution of gas and dust in the galaxy. Unlike Lyα emission, [O II] photons are not resonant in nature; therefore, Lyα/[O II] can be used as an independent measure of Lyα escape. The Lyα and [O II] flux measurements are presented in Section 4.1. The middle panel of Figure 10 shows the distribution of the Lyα/[O II] ratio of LAEs and SFGs. In cases where there is no significant [O II] emission, we have lower limits on the Lyα/[O II] ratio, as shown by the dotted histograms in the figure. We find that log (Lyα/[O II]) ranges from 0.14 to 2.06, with a median ⩾0.91. The distribution also shows that LAEs have higher Lyα/[O II], on average, compared to SFGs due to the higher Lyα escape in LAEs. However, [O II] emission depends on the ionization parameter and metallicity of galaxies, as discussed below.

Figure 11 shows how the intrinsic Lyα/[O II] is predicted to vary with nebular metallicity, Z_{neb}, based on photoionization modeling. To compute this relationship, we use the photoionization modeling code CLOUDY (Ferland et al. 2013) with an intrinsic ionizing spectrum set by the BPASS (Eldridge et al. 2017) constant star formation models, with a stellar metallicity of 0.2 $Z_\odot$ and an age of $10^{7.5}$ yr. We then use these models to compute the expected Lyα/[O II] ratio as a function of Z_{neb}, where the ionization parameter, log(U), is fixed to the value predicted by the anticorrelation between log(U) and Z_{neb} found in local H II regions (Pérez-Montero 2014). As observed in the middle panel of Figure 10, eight LAEs (≈13%) have log (Lyα/[O II]) $\gtrsim$ 1.5, on the high end of what is expected. Because these Lyα/[O II] do not account for the potentially large fraction of Lyα photons that are resonantly scattered out of the photometric aperture, these ratios are effectively lower limits. This suggests that these galaxies are extremes in the parameter space shown in Figure 11. To produce such high Lyα/[O II] ratios, they should have very low nebular metallicities, $Z_{neb} \lesssim 0.2$, and/or very high ionization parameters, log (U) $\gtrsim -2.4$, similar to the values measured for other LAE samples at high redshift (Finkelstein et al. 2011; Nakajima et al. 2012, 2013).

Finally, the Lyα escape fraction ($f_{esc}^{Ly\alpha}$), which is defined as the ratio of the observed Lyα luminosity to the intrinsic Lyα luminosity produced in a galaxy, is the most commonly used parameter to study the escape of Lyα in galaxies. The estimate of the escape fraction depends on several assumptions, such as metallicities, star formation histories, and dust attenuation curves. We calculate the intrinsic Lyα luminosity using the SFR computed from the SED fitting and the CLOUDY models (Ferland et al. 2013). The ionizing photon luminosity per unit SFR for this model is $Q(H^0) = 9.259 \times 10^{-52}\,s^{-1}$. Assuming Case-B recombination, the intrinsic Hα luminosity is $L_{H\alpha}[erg\ s^{-1}] = 1.36 \times 10^{-12}\,Q(H^0)$ (Leitherer & Heckman 1995), and the SFR $[M_\odot\,yr^{-1}] \approx 2.09 \times 10^{-42}\,L(H\alpha)$ [erg s^{-1}] (Reddy et al. 2022). We use this relation to compute the intrinsic Hα luminosity from the SED-based SFR. This assumes that the ionizing photons neither escape nor get absorbed by dust prior to photoionizing hydrogen. Assuming a stellar metallicity of 0.2 $Z_\odot$, an age of $10^{7.5}$ yr, a nebular metallicity of 0.3 $Z_\odot$, and an ionization parameter log(U) of −2.0 yields Lyα/Hα ≈ 8.9 from these models. We use this ratio to compute the intrinsic Lyα luminosity from Hα luminosity, which, along with the observed Lyα luminosities (Section 4.1), is used to calculate $f_{esc}^{Ly\alpha}$ for the LAEs and SFGs.

Three of the LAEs in our sample have computed escape fractions greater than 1. Two of these sources (DENS1_86 and DENS1_356) have extremely faint continua, resulting in poor SED fits. The third source (FIELD4_124) has high Lyα luminosity (≈10^{43} ergs s^{-1}) and is possibly an active galaxy (Sobral et al. 2018; Zhang et al. 2021).

The right panel of Figure 10 shows the distribution of the escape fraction of LAEs in comparison with the SFGs. Given the observed $W_{Ly\alpha}$, these distributions are typical for galaxies at similar and lower redshifts (Matthee et al. 2016; Yang et al. 2017; Weiss et al. 2021; Reddy et al. 2022). The median escape fraction

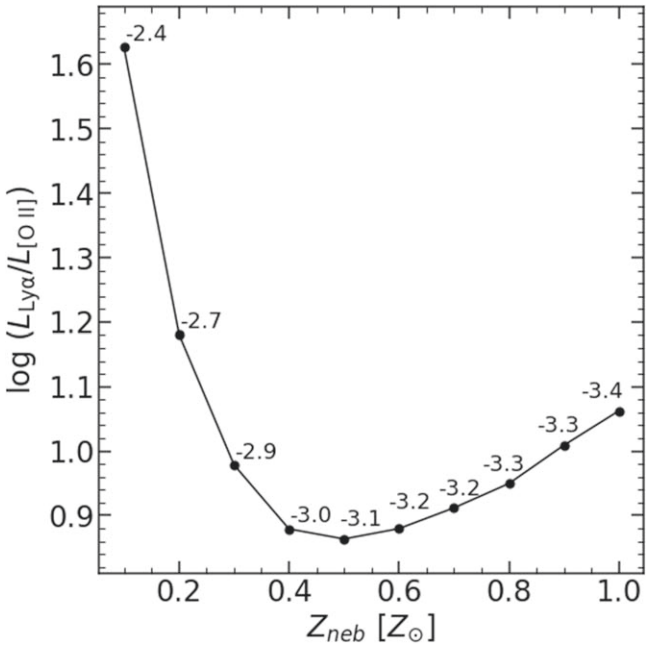

Figure 11. Predicted relationship between Lyα/[O II] and nebular metallicity, Z_{neb}, based on CLOUDY (Ferland et al. 2013) photoionization modeling. This assumes the anticorrelation between the ionization parameter, log(U), and Z_{neb} from Pérez-Montero (2014), with values of the former indicated at each point. See text for further details.

of the SFGs (≈4.8%) is similar to the escape fraction expected at $z \approx 2$–3 (Hayes et al. 2010; Sobral et al. 2017). The LAEs, however, have a median escape fraction of ≈13.5%, which is significantly higher and closer to the escape fraction observed at $z \gtrsim 6$ (see Figures 1 and 4 in Hayes et al. 2011). It has been observed that Lyα escape is correlated with the escape of ionizing photons (Marchi et al. 2017, 2018; Steidel et al. 2018; Pahl et al. 2021), and galaxies with high ionizing escape fractions are often bright LAEs at similar redshifts (Naidu et al. 2022). The comparable escape fractions of the LAEs to the escape fraction observed at $z \gtrsim 6$ suggests that these are probably low-redshift analogs of galaxies that contributed to reionization.

5. Lyα Escape and Galaxy Properties

5.1. Dependence on Stellar Mass and SFR

To understand the physical driver of high Lyα escape in LAEs compared to typical SFGs, we search for any significant trends with galaxy properties. Figure 12 shows how $W_{Ly\alpha}$ and the measured Lyα/[O II] luminosity ratio depend on the stellar masses and SFRs of LAEs and SFGs. In each panel, the filled blue squares and open blue circles represent zLAEs and pLAEs, respectively, and gray crosses denote SFGs. Furthermore, the red square, red circle, and black cross and their corresponding error bars mark the median and interquartile ranges of the individual samples. We study the strength of the correlations using the Spearman correlation test (Table 2). Note that we are not considering $f_{esc}^{Ly\alpha}$ in this analysis, as the calculation of $f_{esc}^{Ly\alpha}$ is dependent on the SFRs derived from the SED fitting. As mentioned in the previous section, we consider $W_{Ly\alpha}$ and Lyα/[O II] as proxies for Lyα escape.

The top panels show $W_{Ly\alpha}$ and Lyα/[O II] as a function of stellar mass. As expected, LAEs have higher $W_{Ly\alpha}$ and Lyα/[O II] ratios. From Table 2, we see that there is a possible anticorrelation between $W_{Ly\alpha}$ and $M_\star$, as well as between Lyα/[O II] and $M_\star$, when we consider both the LAE sample and MOSDEF SFGs together. When we consider the LAE sample alone, there is a moderate anticorrelation between Lyα escape proxies and stellar mass. Focusing on the median points in these panels, we see that Lyα escape has a clear dependence on the stellar mass of SFGs. This is similar to what has been observed in many previous studies (Matthee et al. 2016; Oyarzún et al. 2016, 2017; Santos et al. 2020; Weiss et al. 2021). However, the sample may be incomplete in the lower left regions of these two panels due to the sensitivity limits of both narrowband and continuum-based surveys.

The bottom panels of Figure 12 show the dependence of $W_{Ly\alpha}$ and Lyα/[O II] on the SFR of galaxies. When all LAEs and SFGs are considered, the Spearman ρ coefficient for $W_{Ly\alpha}$ versus SFR is −0.02, while the coefficient for Lyα/[O II] versus SFR is −0.05. This suggests that there is no obvious correlation between Lyα escape and SFR for these galaxies. This nondependence of Lyα escape on SFR is in contrast with several previous studies on LAEs and SFGs (Matthee et al. 2016; Oyarzún et al. 2017; Weiss et al. 2021). This is not surprising because the detection of correlation depends on the dynamic range in Lyα escape and SFR probed by the different samples. As the SFR increases, the intrinsic Lyα emission will increase along with the gas and dust column densities. This increase in gas and dust densities, in turn, will influence the emergent Lyα emission. The observed nondependence of Lyα escape on SFR, along with the diverse range of SFRs in LAEs (Section 4.2.1), suggests that star formation alone is not the primary driver for the escape of Lyα photons. The following subsections discuss the dependence of Lyα escape on sizes and SFR surface densities.

5.2. Dependence on Sizes

Figure 13 shows the dependence of $W_{Ly\alpha}$, the Lyα/[O II] luminosity ratio, and $f_{esc}^{Ly\alpha}$ on the compactness of galaxies. All the points plotted near $r_e \approx 1$ kpc are unresolved galaxies that have sizes $\lesssim$1 kpc. The Lyα escape in LAEs spans a broad range of values and is higher for unresolved galaxies, on average, compared to resolved galaxies. The left and right stars in each of the panels show the median values of the Lyα escape proxies for unresolved and resolved sources, respectively. The error bars denote the interquartile range of the different distributions. These median values suggest a possible 2σ anticorrelation between $f_{esc}^{Ly\alpha}$ and the size of the galaxy.

From Figure 13, we also find that the fraction of resolved pLAEs (≈63%) is higher than the fraction of resolved zLAEs (≈18%). The zLAEs are spectroscopically confirmed due to the stronger Lyα emission from them compared to pLAEs. This also suggests a dependence of $f_{esc}^{Ly\alpha}$ on galaxy sizes.

Bond et al. (2012) studied the rest-frame UV sizes of $z \simeq 2.1$ and 3.1 LAEs and found a systematic trend that higher $W_{Ly\alpha}$ LAEs have smaller median sizes compared to the lower $W_{Ly\alpha}$ samples. This dependence of Lyα escape on galaxy sizes is also seen in typical SFGs. Law et al. (2012) studied ≈200 SFGs and uncovered a higher fraction of Lyα emission in galaxies with compact morphologies. More recently, Weiss et al. (2021) found that $f_{esc}^{Ly\alpha}$ is anticorrelated with r_e for [O III]-emitting galaxies (also see Reddy et al. 2022). Kim et al. (2021) studied nearby green pea galaxies that emit Lyα emission and found that $f_{esc}^{Ly\alpha}$ is dependent on their sizes. Paulino-Afonso et al. (2018) also found an anticorrelation between $W_{Ly\alpha}$ and the UV

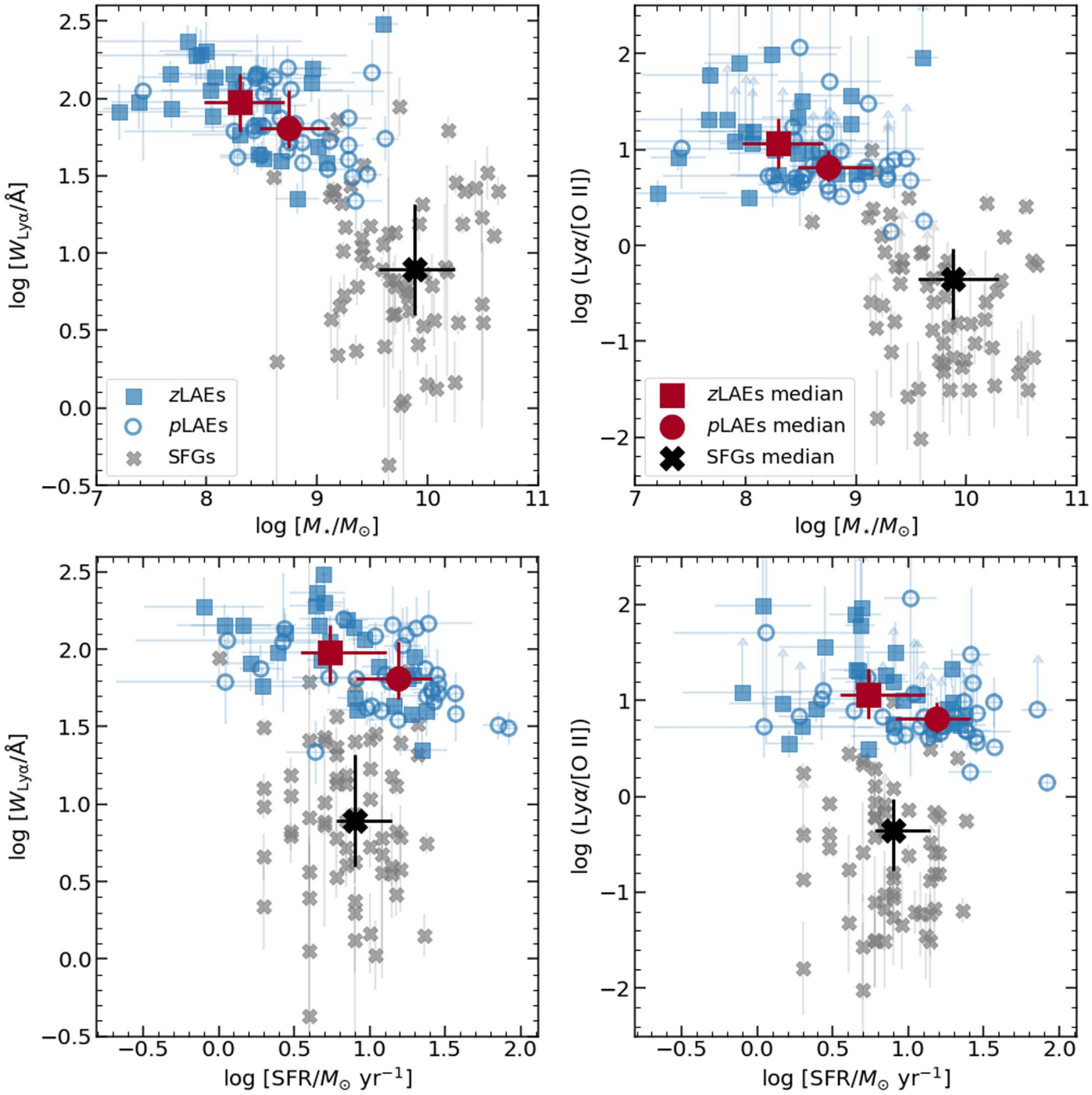

Figure 12. Dependence of $W_{Ly\alpha}$ (left) and Lyα/[O II] luminosity ratio (right) on the stellar mass (top) and SFR (bottom). The *z*LAEs, *p*LAEs, and continuum-selected SFGs are shown as filled blue squares, open blue circles, and gray crosses, respectively. The red square, red circle, and black cross along with their corresponding error bars are the median and interquartile range for the subsets.

Table 2
Spearman ρ Parameter for Different Correlations

Proxy for Lyα Escape	log ($M_\star$ ($M_\odot$))		log (SFR ($M_\odot$ yr^{-1}))	
	Only LAEs	LAEs+MOSDEF	Only LAEs	LAEs+MOSDEF
$W_{Ly\alpha}$	−0.47 (0.0001)	−0.72 (1.4×10^{-21})	−0.50 (2.9×10^{-5})	−0.02 (0.80)
Lyα/[O II]	−0.24 (0.06)	−0.73 (7.4×10^{-19})	−0.39 (0.002)	−0.05 (0.59)

Note. The *p*-values for each of the parameters are shown in parentheses.

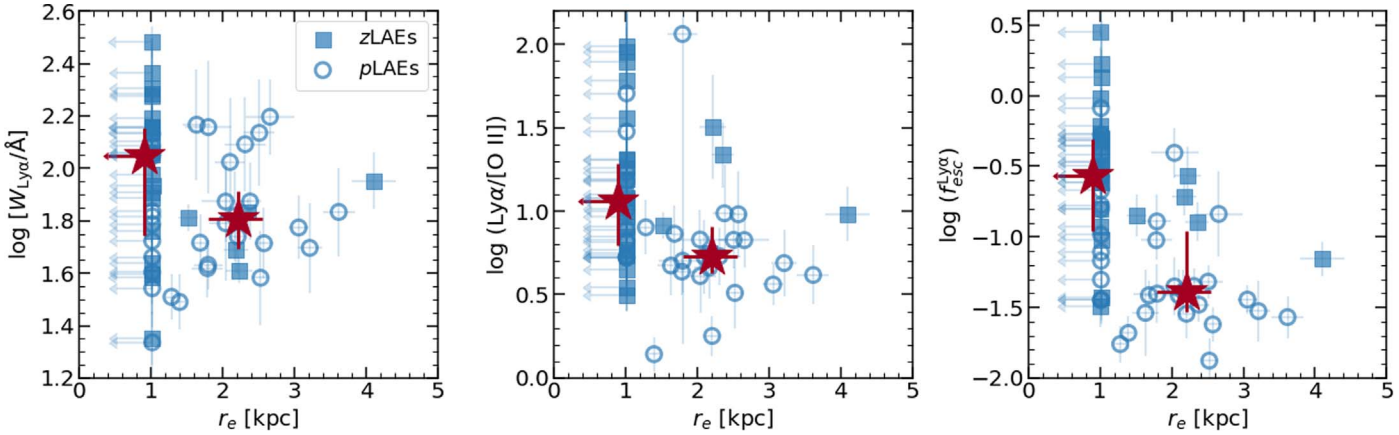

Figure 13. Equivalent width, $W_{Ly\alpha}$ (left); Lyα/[O II] luminosity ratio (middle); and escape fraction, $f_{esc}^{Ly\alpha}$ (right), as a function of effective radius r_e. The symbols and colors are the same as in Figure 12. In each panel, the left and right stars are the median values for the unresolved and resolved sources, respectively. The error bars denote the interquartile ranges for the individual parameters.

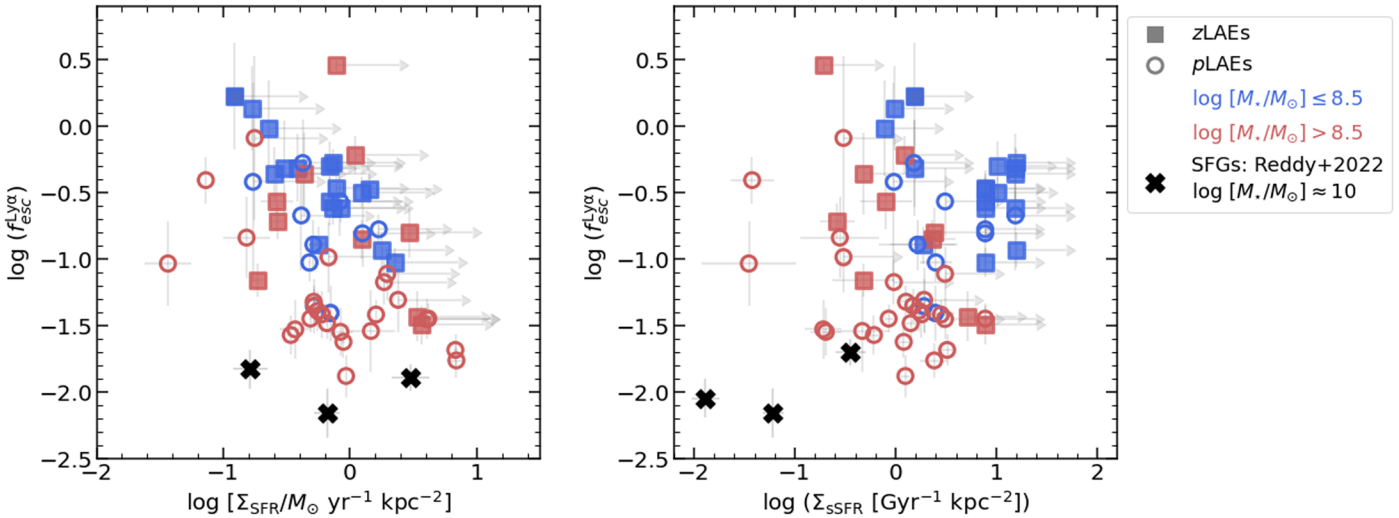

Figure 14. Escape fraction as a function of SFR surface density, Σ_{SFR} (left), and sSFR surface density, Σ_{sSFR} (right). The filled squares and open circles are *z*LAEs and *p*LAEs, respectively. Low-mass LAEs (log $[M_*/M_\odot] \leqslant 8.5$) are shown in blue, while high-mass LAEs (log $[M_*/M_\odot] > 8.5$) are shown in red. The black crosses are from Reddy et al. (2022) and computed using the composite spectra of the SFGs.

sizes of high-redshift LAEs in the range $2 \lesssim z \lesssim 6$. These studies suggest that this dependence is independent of redshift. Therefore, galaxy sizes clearly play an important role in the escape of Lyα photons.

5.3. Dependence on SFR Surface Densities

Observational studies suggest a possible correlation between the Lyα escape fraction and Σ_{SFR} (Heckman et al. 2011; Verhamme et al. 2017; Marchi et al. 2019; Reddy et al. 2022). Furthermore, the gravitational potential of the galaxy, encoded in sSFR surface density, Σ_{sSFR}, can also influence the escape of Lyα photons. In Figure 14, we compare our sample of LAEs with those obtained for MOSDEF SFGs from Reddy et al. (2022; similar to their Figure 21). The *z*LAEs and *p*LAEs are shown as filled squares and open circles, respectively. We further divide the LAEs into low-mass (log$[M_*/M_\odot] \leqslant 8.5$) and high-mass (log $[M_*/M_\odot] > 8.5$) sources, shown by blue and red symbols, respectively. The SFGs have a median stellar mass, log $[M_*/M_\odot] \approx 10$.

In Figure 14, the LAEs that have only lower limits to their Σ_{SFR} and Σ_{sSFR} are the sources that are unresolved, with sizes $\lesssim$1 kpc. From the left panel, we see that the sources that are resolved have similar Σ_{SFR} but higher $f_{esc}^{Ly\alpha}$ compared to SFGs. This suggests that there is an additional factor beyond Σ_{SFR} that modulates $f_{esc}^{Ly\alpha}$. For galaxies with a fixed Σ_{SFR}, we see that the sources with lower masses have higher $f_{esc}^{Ly\alpha}$. This can also be seen from the right panel of the figure, where LAEs have higher Σ_{sSFR}, on average, compared to SFGs. This highlights the effect of stellar mass (and therefore the gravitational potential) on the Lyα escape (Section 5.1 and Figure 12).

These results reinforce the argument that the distribution of star formation is a key ingredient for Lyα escape. The feedback associated with compact star formation will lead to outflows that will, in turn, create low-density channels in the ISM. These low-density columns provide pathways for the Lyα photons to propagate and escape. The gravitational potential (or stellar mass) also plays a crucial role in this scenario. The shallow potential well of low-mass sources makes it harder for them to retain the gas that is pushed out via winds and outflows. As we are measuring the Lyα photons along the line of sight, this physical interpretation is highly dependent on the orientation of galaxies. Large-scale deep observations of galaxies across the multi-wavelength regime will give further clues about the dependence of Lyα escape on gravitational potential and the sizes of galaxies.

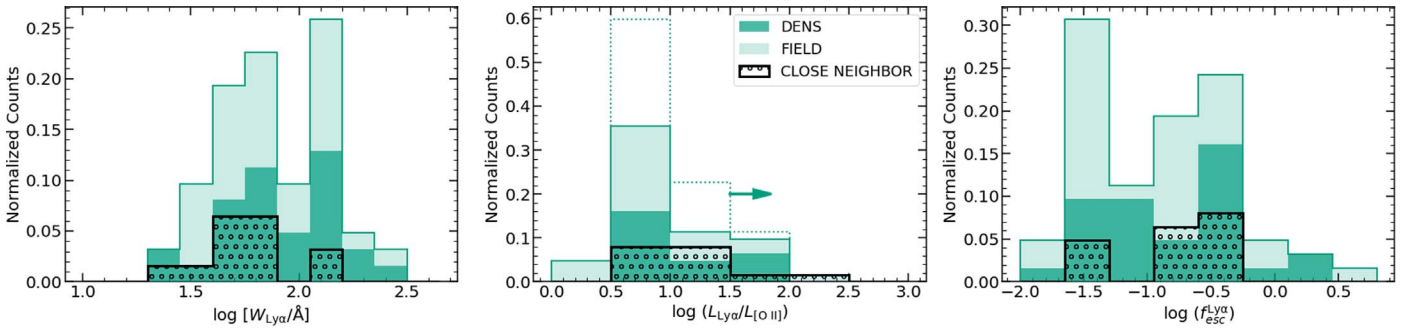

Figure 15. Distribution of $W_{Ly\alpha}$ (left), the Lyα/[O II] ratio (middle), and $f_{esc}^{Ly\alpha}$ (right) for LAEs in the DENS (dark green histograms) and FIELD (light green histograms) regions. The black histograms with circles are 14 LAEs that have close neighbors or extended features as seen visually in the HST images.

Table 3
p-values from K-S Test between Sources in DENS and FIELD Regions

LAE Group	log ($M_\star/M_\odot$)	SFR ($M_\odot$ yr^{-1})	log (f_{esc})	log ($W_{Ly\alpha}$)	log (Lyα/[O II])
zLAEs	0.35	0.45	0.27	0.98	0.61
All LAEs	0.18	0.39	0.17	0.51	0.89

5.4. Dependence on the Environment

In this subsection, we investigate whether Lyα escape has any dependence on the environment of LAEs. In Section 2.1, we mention that we have HST imaging of LAEs in seven fields, three of which are in dense regions, as measured by Prescott et al. (2008). Thus, we divide our LAEs into high-density (DENS) and low-density (FIELD) sources based on their proximity to the LAB. Some LAE candidates either have a close companion or exhibit an extended component visible in the HST images. These companions and/or components are typically not resolved in the ground-based images and may indicate a close physical companion. Out of the 62 LAEs in our sample, we identify 14 sources that exhibit such components within 1.″5. We consider the Lyα escape of this subset in comparison with the rest of the LAEs.

Figure 15 shows the distribution of different Lyα escape proxies for LAEs in low- and high-density environments. The dark and light green histograms are LAEs in the DENS and FIELD regions, respectively. We perform K-S tests for the different proxies between all LAEs in these two groups. We also repeat the tests by considering just the zLAEs, since the spectroscopic redshifts yield more accurate environmental information (Table 3). From the p-values, we cannot reject the null hypothesis that the Lyα escape for DENS and FIELD regions is similar. Additionally, the black histograms with circles in the figure indicate the LAEs with close neighbors and/or extended components. The p-values from the K-S tests between these 14 LAEs and the rest of the LAEs for $W_{Ly\alpha}$, the Lyα/[O II] ratio, and $f_{esc}^{Ly\alpha}$ are 0.26, 0.35, and 0.42, respectively. This suggests that, given our rough definition of environment, Lyα escape does not depend on the local environment of the LAEs in this sample.

Table 3 also shows the p-values from the K-S tests for stellar masses and SFRs between LAEs in the DENS and FIELD regions. For both zLAEs and all LAEs together, we find that the stellar masses and SFRs are statistically similar for LAEs in these different environments. We cannot make any comparisons between the sizes of these galaxies because of the high fraction of unresolved sources and small number of resolved LAEs in the individual groups. However, given that most of the LAEs in our sample are compact, the Σ_{sSFR} of the LAEs in the DENS and FIELD environments are likely similar. This argument supports our earlier result that the star formation in a low-mass, compact galaxy is key to the Lyα escape in galaxies, irrespective of the local environment.

6. Conclusions

In an effort to understand the mechanisms that lead to Lyα escape in LAEs, we study 62 LAEs from seven HST fields using multiwavelength photometry. Of these, 27 sources have confirmed spectroscopic redshifts in the range $2.55 \leqslant z \leqslant 2.75$. In addition to broadband photometry in the B_W, R, I, F110W, and F160W filters, we also have medium-band photometry in the IA445 and F139M bands that probe the Lyα and [O II] emission lines, respectively, in this redshift range. We considered a comparison sample of 136 typical SFGs that are part of the MOSDEF/LRIS sample (Section 2.2).

We obtained the stellar masses, SFRs, ages, and dust content of all the LAEs using the SED fitting technique (Section 4.2). We also computed LAE sizes by running GALFIT on the HST F110W images (Section 4.3). Finally, we considered three proxies for the Lyα escape: the Lyα equivalent width ($W_{Ly\alpha}$), the Lyα/[O II] luminosity ratio, and the Lyα escape fraction ($f_{esc}^{Ly\alpha}$; Section 4.4). Using these proxies and studying their correlations with the LAE properties, we conclude the following.

1. The LAEs typically probe low-mass ($7.2 \leqslant \log(M_\star/M_\odot) \leqslant 9.6$), young (age $\leqslant 1$ Gyr) SFGs ($0.8\ M_\odot$ yr^{-1} $\leqslant$SFR $\leqslant 100\ M_\odot$ yr^{-1}) with low dust content ($E(B-V) \leqslant 0.26$ mag). The pLAEs are more massive, star-forming, older, and redder compared to zLAEs. Furthermore, LAEs and SFGs have different underlying distributions. The LAEs have lower ages, lower masses, similar SFRs, and less dust content compared to SFGs at similar redshifts (Section 4.2.1).
2. The LAEs have a wide range of SFRs and higher sSFRs compared to SFGs. On average, less massive LAEs lie above the SFMS, compared to their massive counterparts (Section 4.2.2).

3. Almost 60% of the LAEs are unresolved, even with HST resolution, indicating that these galaxies are compact ($r_e \leqslant 1$ kpc). The LAEs also have comparable $\Sigma_{\rm SFR}$ and higher $\Sigma_{\rm sSFR}$ compared to SFGs (Section 4.3).
4. The LAEs have higher $W_{\rm Ly\alpha}$, Lyα/[O II] luminosity ratios, and $f_{\rm esc}^{\rm Ly\alpha}$ compared to SFGs. By comparing the Lyα/[O II] ratios with expected model values, we found that some LAEs are extreme galaxies with low nebular metallicities ($Z_{\rm neb} \lesssim 0.2\ Z_{\odot}$) and/or high ionization parameters ($\log(U) \gtrsim -2.4$). Additionally, the $f_{\rm esc}^{\rm Ly\alpha}$ of LAEs is similar to the escape fraction observed at $z \gtrsim 6$, suggesting that these LAEs may be low-redshift analogs of galaxies that contributed to reionization (Section 4.4).
5. The escape of Lyα in galaxies is anticorrelated with stellar mass but shows no obvious dependence on SFR (Section 5.1).
6. The Lyα escape has a wide range of values for unresolved LAEs and is, on average, higher for unresolved LAEs compared to their resolved counterparts (Section 5.2).
7. For a given $\Sigma_{\rm SFR}$, the lower-mass LAEs have a higher $f_{\rm esc}^{\rm Ly\alpha}$ than their more massive counterparts. This is consistent with a scenario where compact star formation in a low gravitational potential facilitates the escape of Lyα by creating low column density channels in the ISM via feedback (Section 5.3).
8. Based on the local density of the HST fields, we do not observe any obvious dependence of the nearby environment on the Lyα escape from galaxies (Section 5.4).

Upcoming surveys, such as the One-hundred square-degree DECam Imaging in Narrowbands (ODIN) survey, the Legacy Survey of Space and Time with the Vera Rubin Telescope (Ivezić et al. 2019), and deep JWST NIRSPEC observations (Giardino et al. 2016), will provide us with large-scale observations of LAEs in different environments across different epochs. These new data sets will help us understand the physics of Lyα escape in more detail.

We thank the anonymous referee for thoroughly reading the manuscript and helping us improve this work. The authors thank the MOSDEF team for providing [O II] measurements and SED parameters for the comparison SFG sample. We also thank Ryan Sanders, Alice Shapley, and Michael Topping for providing data from the follow-up LRIS observations of MOSDEF galaxies. R.P. also thanks Gurtina Besla, Ryan Endsley, Xiaohui Fan, and Rob Kennicutt for their helpful comments on this project.

This research is primarily the result of observations from the Hubble Space Telescope and was supported by HST-GO-13000 (PI: Sungryong Hong). R.P. was supported by the University of Arizona and in part by NOIRLab, which is managed by the Association of Universities for Research in Astronomy (AURA). A.D.'s and S.J.'s research is supported by NSF's NOIRLab, which is operated by the Association of Universities for Research in Astronomy (AURA) under a cooperative agreement with the National Science Foundation. A.D.'s research is also supported in part by a fellowship from the John Simon Guggenheim Memorial Foundation and by the Institute of Theory and Computation at the Harvard-Smithsonian Center for Astrophysics. M.K.M.P acknowledges support from NSF grant AAG-1813016. The authors also acknowledge financial support from NASA through the Astrophysics Data Analysis Program, grant No. 80NSSC19K0582, and from NSF AST Award #2206705.

The research also made use of observations from the NOAO Deep Wide-Field Survey (NDWFS; NOAO Prop. ID No. 1999B-0027; Co-PIs: B. Jannuzi and A. Dey), which used observations made with the Mosaic-3 camera at the Mayall 4 m telescope at Kitt Peak National Observatory, National Optical Astronomy Observatory, which is operated by the Association of Universities for Research in Astronomy (AURA) under cooperative agreement with the National Science Foundation. The authors are honored to be permitted to conduct astronomical research on Iolkam Du'ag (Kitt Peak), a mountain with particular significance to the Tohono O'odham.

This research is based in part on data collected at the Subaru Telescope, which is operated by the National Astronomical Observatory of Japan. We are honored and grateful for the opportunity of observing the universe from Maunakea, which has cultural, historical, and national significance in Hawaii.

Some of the data presented in this paper were obtained from the Mikulski Archive for Space Telescopes (MAST) at the Space Telescope Science Institute. These observations can be accessed via https://doi.org/10.17909/48vk-jr50.

Facilities: HST (WFC3), Mayall, Subaru (SuprimeCam).

Software: AstroDrizzle, Astropy, GALFIT, IRAF, Matplotlib, NumPy, SExtractor.

Appendix

We present the properties of all the LAEs studied in this paper here. Figures 16 and 17 show the image cutouts ($10'' \times 10''$) of *z*LAEs and *p*LAEs, respectively, in all the seven bands (B_w, IA445, R, I, F110W, F139M, and F160W from left to right). The green circles within each of the panels show the apertures used for photometry within each band. Majority of the LAEs have a faint continuum, but with a bright emission in the IA445, corresponding to the Lyα emission. Table 4 shows the coordinates, redshifts, and photometric information for the LAEs. The SED-based measurements, along the emission-line measurements is shown in Table 5. Tables 6 and 7 show the size measurement and Ly*a* escape proxies of the LAEs, respectively.

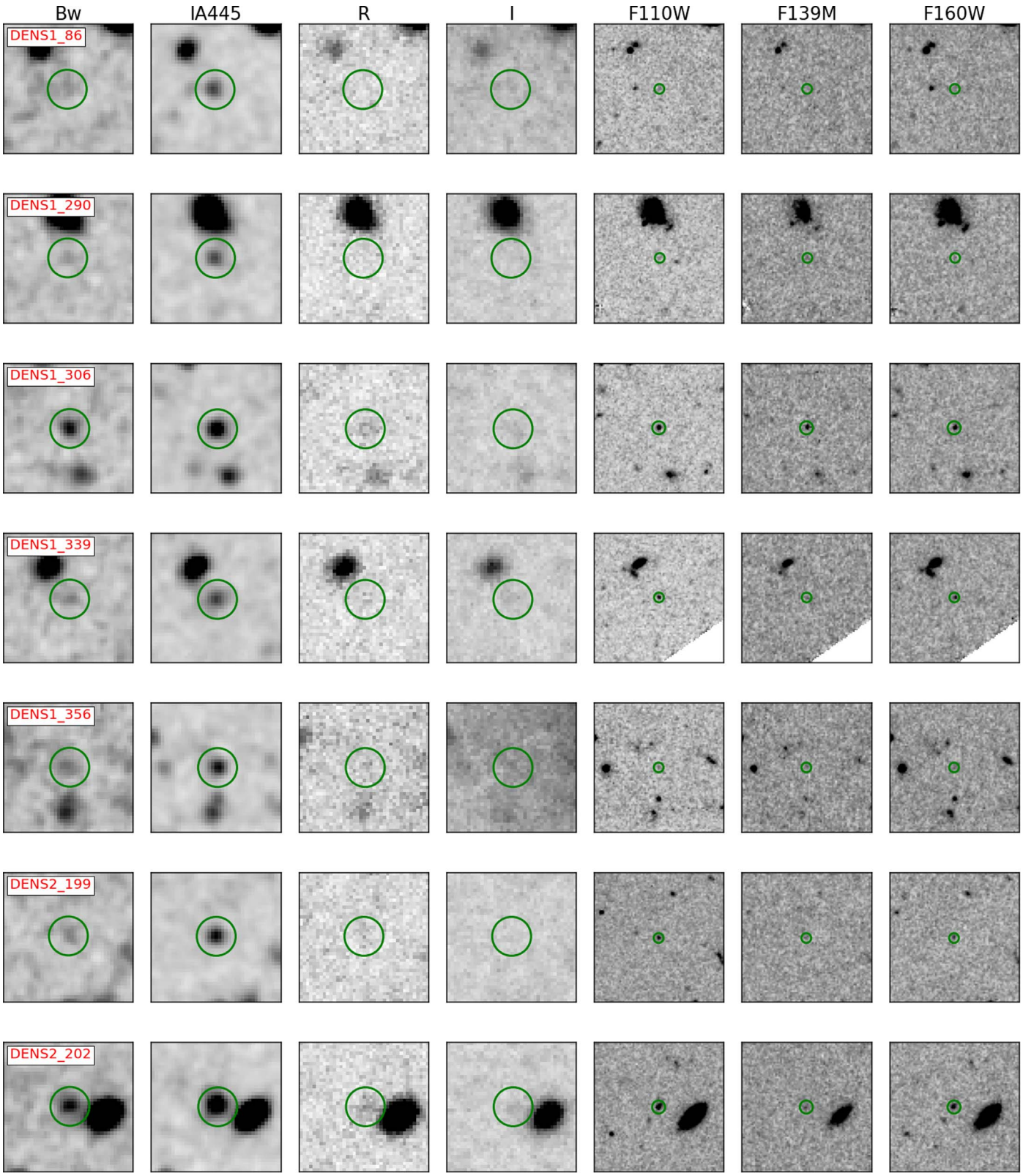

Figure 16. Image cutouts ($10'' \times 10''$) of zLAEs in B_W, IA445, R, I, F110W, F139M, and F160W (left to right). The green circles denote the apertures used for performing photometry.

(An extended version of this figure is available.)

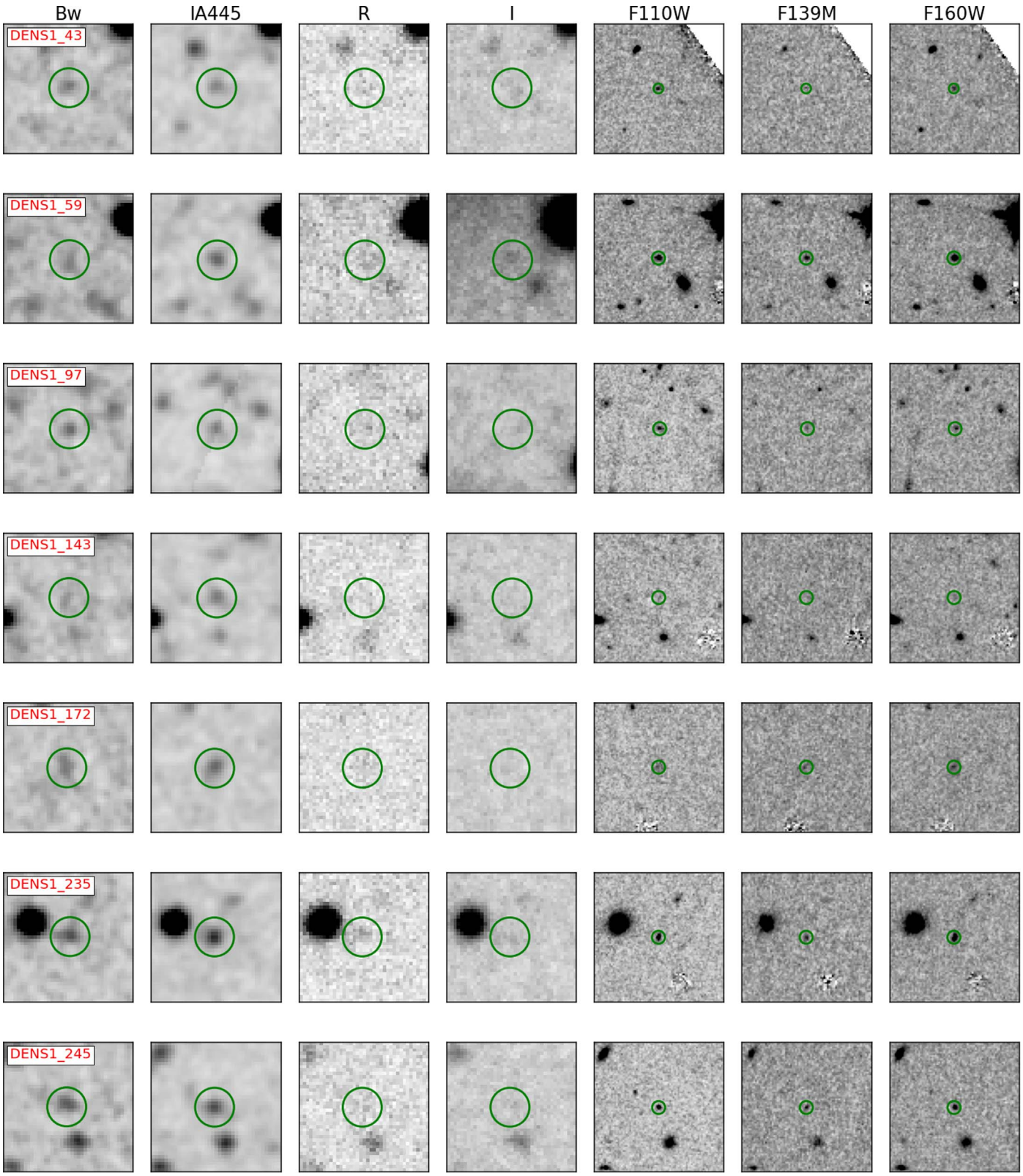

Figure 17. Image cutouts ($10'' \times 10''$) of *p*LAEs in B_W, IA445, R, I, F110W, F139M, and F160W (left to right). The green circles denote the apertures used for performing photometry.

(An extended version of this figure is available.)

Table 4
Position and Photometry of the LAEs

ID	R.A.	Decl.	z_{spec}	B_W	IA445	R	I	F110W	F139M	F160W
					*z*LAEs					
DENS1_86	218.54699	33.33212	2.6599	26.89 ± 0.32	25.59 ± 0.09	28.13 ± 1.48	28.16 ± 1.87	27.87 ± 0.46	27.76 ± 1.00	27.52 ± 0.40
DENS1_290	218.54867	33.31537	2.6890	27.10 ± 0.37	25.52 ± 0.08	26.63 ± 0.62	25.93 ± 0.51	28.32 ± 0.64	26.82 ± 0.55	28.43 ± 0.75
DENS1_306	218.54201	33.31323	2.6593	25.58 ± 0.10	24.94 ± 0.05	25.52 ± 0.26	25.43 ± 0.36	25.37 ± 0.08	25.01 ± 0.17	25.45 ± 0.10
DENS1_339	218.53821	33.30828	2.6905	26.47 ± 0.22	25.30 ± 0.07	26.15 ± 0.43	25.35 ± 0.33	26.24 ± 0.12	26.97 ± 0.61	26.12 ± 0.13
DENS1_356	218.54893	33.33707	2.6662	26.54 ± 0.24	25.41 ± 0.08	27.41 ± 0.75	28.49 ± 2.17	27.78 ± 0.43	27.13 ± 0.67	26.94 ± 0.25
DENS2_199	218.54365	33.26862	2.6650	26.61 ± 0.25	25.34 ± 0.08	28.90 ± 2.12	26.84 ± 0.75	26.65 ± 0.09	27.09 ± 0.65	26.79 ± 0.22
DENS2_202	218.53539	33.26821	2.6638	25.15 ± 0.07	24.40 ± 0.03	24.97 ± 0.17	25.03 ± 0.25	25.62 ± 0.05	25.39 ± 0.22	25.44 ± 0.09
DENS2_235	218.55726	33.26553	2.6630	26.80 ± 0.29	25.07 ± 0.06	27.14 ± 0.88	26.52 ± 0.79	27.02 ± 0.13	27.21 ± 0.70	26.96 ± 0.26
DENS3_17	218.49395	33.31581	2.6615	27.17 ± 0.39	25.98 ± 0.13	26.68 ± 0.65	27.51 ± 1.39	27.85 ± 0.27	26.56 ± 0.45	29.27 ± 1.30
DENS3_41	218.50143	33.31221	2.6172	25.49 ± 0.10	25.00 ± 0.06	25.17 ± 0.20	24.70 ± 0.20	25.00 ± 0.03	25.11 ± 0.18	24.79 ± 0.05
DENS3_118	218.51525	33.30501	2.6443	26.72 ± 0.28	25.55 ± 0.09	26.66 ± 0.64	28.48 ± 2.20	26.44 ± 0.11	26.01 ± 0.37	25.91 ± 0.14
DENS3_285	218.50141	33.28827	2.6509	26.34 ± 0.20	25.50 ± 0.09	26.14 ± 0.43	26.86 ± 0.97	26.83 ± 0.16	26.00 ± 0.37	26.54 ± 0.23
FIELD1_45	218.19319	33.25234	2.6700	25.41 ± 0.10	24.26 ± 0.03	25.83 ± 0.35	27.00 ± 1.30	25.55 ± 0.06	25.05 ± 0.17	25.25 ± 0.08
FIELD1_89	218.18495	33.24749	2.6863	26.59 ± 0.28	25.48 ± 0.09	27.45 ± 0.75	26.85 ± 1.16	26.98 ± 0.22	27.37 ± 0.75	26.68 ± 0.27
FIELD1_122	218.19026	33.24321	2.7191	26.50 ± 0.26	24.90 ± 0.05	25.95 ± 0.39	26.77 ± 0.75	26.90 ± 0.14	30.90 ± 3.66	28.12 ± 0.64
FIELD1_180	218.19246	33.23632	2.6678	25.34 ± 0.10	24.51 ± 0.04	25.18 ± 0.20	25.59 ± 0.53	25.14 ± 0.04	24.74 ± 0.13	24.97 ± 0.06
FIELD1_265	218.19829	33.22367	2.6958	26.23 ± 0.21	25.50 ± 0.09	27.41 ± 1.08	27.22 ± 1.44	26.38 ± 0.13	25.49 ± 0.24	26.71 ± 0.27
FIELD1_281	218.18990	33.25455	2.6859	27.30 ± 0.49	25.74 ± 0.11	27.45 ± 0.75	26.77 ± 0.75	26.93 ± 0.15	26.97 ± 0.62	27.16 ± 0.31
FIELD2_64	217.76887	33.18873	2.6766	26.18 ± 0.21	25.55 ± 0.12	25.96 ± 0.38	25.30 ± 0.44	25.26 ± 0.04	25.04 ± 0.17	25.12 ± 0.07
FIELD2_91	217.78369	33.18538	2.6773	25.66 ± 0.13	24.56 ± 0.05	25.20 ± 0.20	24.77 ± 0.29	25.42 ± 0.04	25.16 ± 0.19	25.25 ± 0.08
FIELD2_132	217.78603	33.18136	2.7051	25.64 ± 0.13	24.95 ± 0.07	25.55 ± 0.29	25.70 ± 0.58	25.47 ± 0.05	24.95 ± 0.16	25.14 ± 0.07
FIELD2_174	217.80338	33.17495	2.7036	24.76 ± 0.06	24.08 ± 0.03	24.55 ± 0.12	24.42 ± 0.21	24.71 ± 0.02	24.27 ± 0.09	24.51 ± 0.04
FIELD3_124	218.08984	33.34466	2.7400	25.89 ± 0.16	24.90 ± 0.06	26.68 ± 0.69	27.76 ± 1.88	26.17 ± 0.10	26.20 ± 0.44	26.19 ± 0.18
FIELD3_327	218.10093	33.31795	2.5950	26.15 ± 0.19	25.41 ± 0.09	26.92 ± 0.77	26.78 ± 0.75	26.72 ± 0.12	26.70 ± 0.50	26.87 ± 0.24
FIELD4_33	218.24553	33.68381	2.6186	25.61 ± 0.17	24.48 ± 0.04	25.90 ± 0.44	25.78 ± 0.56	25.83 ± 0.09	25.29 ± 0.21	25.93 ± 0.14
FIELD4_50	218.24910	33.68082	2.6272	26.15 ± 0.26	25.27 ± 0.09	26.30 ± 0.59	26.10 ± 0.72	25.48 ± 0.06	25.15 ± 0.18	25.27 ± 0.08
FIELD4_124	218.25557	33.66906	2.7122	24.64 ± 0.06	23.18 ± 0.01	26.05 ± 0.50	26.78 ± 1.10	25.61 ± 0.07	25.70 ± 0.29	24.74 ± 0.05
					*p*LAEs					
DENS1_43	218.52519	33.33647	⋯	27.74 ± 0.60	26.44 ± 0.19	27.41 ± 0.75	27.12 ± 1.10	26.18 ± 0.12	26.70 ± 0.50	25.96 ± 0.11
DENS1_59	218.53597	33.33473	⋯	27.49 ± 0.50	26.20 ± 0.15	26.99 ± 0.77	26.76 ± 0.75	25.36 ± 0.08	24.81 ± 0.14	24.73 ± 0.05
DENS1_97	218.56296	33.33126	⋯	27.26 ± 0.42	26.03 ± 0.13	26.71 ± 0.64	26.76 ± 0.75	25.58 ± 0.10	25.96 ± 0.35	25.87 ± 0.13
DENS1_143	218.53259	33.32746	⋯	27.26 ± 0.42	26.41 ± 0.18	27.41 ± 0.75	26.70 ± 0.88	27.54 ± 0.49	26.70 ± 0.62	27.03 ± 0.36
DENS1_172	218.52629	33.32519	⋯	26.47 ± 0.23	25.80 ± 0.11	26.32 ± 0.49	30.13 ± 3.67	25.72 ± 0.11	25.18 ± 0.19	25.29 ± 0.08
DENS1_235	218.54419	33.32148	⋯	26.10 ± 0.17	25.46 ± 0.08	25.93 ± 0.37	25.10 ± 0.27	25.26 ± 0.07	25.27 ± 0.21	24.78 ± 0.05
DENS1_245	218.55910	33.32026	⋯	26.24 ± 0.19	25.54 ± 0.09	26.65 ± 0.64	25.68 ± 0.43	25.56 ± 0.10	25.54 ± 0.26	25.28 ± 0.08
DENS1_266	218.55763	33.31803	⋯	26.24 ± 0.19	25.66 ± 0.10	25.66 ± 0.29	25.44 ± 0.36	25.82 ± 0.12	25.32 ± 0.21	25.17 ± 0.07
DENS1_304	218.55536	33.31371	⋯	27.96 ± 0.70	26.35 ± 0.17	27.41 ± 0.75	26.76 ± 0.75	27.88 ± 0.63	27.27 ± 0.75	27.93 ± 0.68
DENS1_344	218.54156	33.30592	⋯	26.34 ± 0.20	25.40 ± 0.08	27.25 ± 0.92	27.19 ± 1.15	26.53 ± 0.22	26.02 ± 0.38	26.33 ± 0.20
DENS2_24	218.54337	33.28530	⋯	26.57 ± 0.24	25.85 ± 0.12	26.86 ± 0.74	25.89 ± 0.50	25.40 ± 0.04	25.21 ± 0.20	25.27 ± 0.08
DENS2_239	218.56262	33.26529	⋯	27.16 ± 0.39	25.86 ± 0.13	27.31 ± 0.75	26.84 ± 0.75	26.32 ± 0.10	26.50 ± 0.54	25.90 ± 0.14
DENS2_281	218.57589	33.26184	⋯	26.01 ± 0.15	25.36 ± 0.08	25.85 ± 0.36	25.89 ± 0.50	25.87 ± 0.07	25.52 ± 0.26	26.03 ± 0.16
DENS3_20	218.49754	33.31536	⋯	26.64 ± 0.26	25.97 ± 0.13	26.01 ± 0.39	25.18 ± 0.29	24.84 ± 0.03	24.87 ± 0.15	24.88 ± 0.06
DENS3_126	218.51845	33.30441	⋯	26.13 ± 0.17	25.48 ± 0.09	25.95 ± 0.38	25.74 ± 0.44	24.99 ± 0.03	24.76 ± 0.13	24.66 ± 0.05
DENS3_172	218.50684	33.29998	⋯	26.89 ± 0.31	25.82 ± 0.12	27.38 ± 1.02	26.82 ± 0.75	27.08 ± 0.20	26.62 ± 0.59	26.50 ± 0.23
DENS3_279	218.51691	33.28891	⋯	26.82 ± 0.30	25.89 ± 0.12	26.46 ± 0.55	27.16 ± 1.15	26.52 ± 0.09	27.32 ± 0.76	25.81 ± 0.10

Table 4
(Continued)

ID	R.A.	Decl.	z_{spec}	B_W	IA445	R	I	F110W	F139M	F160W
FIELD1_60	218.21814	33.25018	⋯	26.74 ± 0.32	25.94 ± 0.13	26.60 ± 0.63	26.01 ± 0.72	25.63 ± 0.07	25.79 ± 0.31	25.72 ± 0.12
FIELD1_71	218.21986	33.24939	⋯	27.12 ± 0.43	26.20 ± 0.16	27.73 ± 1.27	25.89 ± 0.65	25.59 ± 0.06	25.69 ± 0.29	26.19 ± 0.18
FIELD1_270	218.20566	33.22301	⋯	26.46 ± 0.25	25.75 ± 0.11	26.07 ± 0.42	25.73 ± 0.60	24.83 ± 0.03	24.23 ± 0.08	24.27 ± 0.03
FIELD1_283	218.20151	33.25264	⋯	24.97 ± 0.07	24.46 ± 0.09	24.69 ± 0.14	24.10 ± 0.16	23.81 ± 0.01	23.38 ± 0.04	23.70 ± 0.02
FIELD2_26	217.78132	33.19250	⋯	26.02 ± 0.19	25.09 ± 0.08	25.67 ± 0.32	26.34 ± 0.90	26.13 ± 0.08	25.79 ± 0.32	25.93 ± 0.14
FIELD2_29	217.79498	33.19222	⋯	26.04 ± 0.19	25.43 ± 0.10	25.64 ± 0.31	25.40 ± 0.47	25.20 ± 0.04	24.87 ± 0.15	24.86 ± 0.06
FIELD2_71	217.77752	33.18753	⋯	26.70 ± 0.32	25.83 ± 0.15	26.18 ± 0.45	26.13 ± 0.77	25.23 ± 0.04	24.96 ± 0.16	25.13 ± 0.07
FIELD2_116	217.79680	33.18165	⋯	27.00 ± 0.39	26.03 ± 0.18	26.41 ± 0.55	25.77 ± 0.60	25.87 ± 0.07	26.00 ± 0.37	25.92 ± 0.14
FIELD2_140	217.78061	33.17919	⋯	25.31 ± 0.10	24.85 ± 0.06	24.99 ± 0.18	24.81 ± 0.30	23.97 ± 0.01	24.01 ± 0.07	23.71 ± 0.02
FIELD2_141	217.78641	33.17908	⋯	25.82 ± 0.15	25.28 ± 0.09	25.99 ± 0.40	25.79 ± 0.63	25.01 ± 0.03	25.07 ± 0.17	24.89 ± 0.06
FIELD2_149	217.76941	33.17862	⋯	28.94 ± 1.09	25.84 ± 0.08	29.43 ± 2.30	27.38 ± 0.75	26.51 ± 0.12	25.78 ± 0.31	26.55 ± 0.24
FIELD2_181	217.77873	33.17458	⋯	26.26 ± 0.22	25.52 ± 0.11	25.83 ± 0.35	25.47 ± 0.50	24.93 ± 0.03	24.75 ± 0.13	24.78 ± 0.05
FIELD2_243	217.78797	33.16508	⋯	26.18 ± 0.20	25.43 ± 0.10	26.17 ± 0.46	25.12 ± 0.38	25.01 ± 0.03	24.74 ± 0.13	25.02 ± 0.06
FIELD2_253	217.78553	33.16276	⋯	26.55 ± 0.27	25.73 ± 0.14	25.99 ± 0.40	25.10 ± 0.38	25.06 ± 0.03	24.96 ± 0.15	24.61 ± 0.04
FIELD2_257	217.78823	33.16198	⋯	25.97 ± 0.17	25.36 ± 0.10	25.85 ± 0.36	25.42 ± 0.47	25.05 ± 0.03	24.95 ± 0.15	25.00 ± 0.06
FIELD3_173	218.09895	33.33332	⋯	26.05 ± 0.18	25.11 ± 0.07	26.62 ± 0.62	26.78 ± 0.75	25.84 ± 0.08	25.92 ± 0.36	25.84 ± 0.14
FIELD3_311	218.07962	33.32042	⋯	26.80 ± 0.33	25.83 ± 0.13	27.81 ± 1.32	26.00 ± 0.70	25.45 ± 0.05	25.53 ± 0.25	25.52 ± 0.10
FIELD4_127	218.23677	33.66879	⋯	25.62 ± 0.17	24.96 ± 0.06	25.54 ± 0.37	25.52 ± 0.45	25.63 ± 0.07	25.51 ± 0.25	25.47 ± 0.10

Table 5
Properties of the LAEs

ID	log ($M_\star$ ($M_\odot$))	SFR ($M_\odot$ yr^{-1})	Age (Myr)	$E(B-V)$ (mag)	$L_{\mathrm{Ly}\alpha}$ (10^{42} ergs s^{-1})	$L_{(\mathrm{O\ II})}$ (10^{41} ergs s^{-1})
			*z*LAEs			
DENS1_86	7.9 ± 1.4	0.8 ± 0.7	101.0 ± 518.6	0.00 ± 0.02	2.99 ± 0.44	<2.5
DENS1_290	7.4 ± 0.2	2.5 ± 1.4	10.0 ± 0.5	0.01 ± 0.03	2.69 ± 0.51	3.3 ± 0.8
DENS1_306	8.5 ± 0.2	14.6 ± 3.1	19.0 ± 21.8	0.06 ± 0.01	3.10 ± 0.40	6.9 ± 1.1
DENS1_339	8.1 ± 0.3	11.4 ± 2.9	10.0 ± 24.3	0.08 ± 0.03	3.03 ± 0.43	<2.6
DENS1_356	8.2 ± 0.6	1.1 ± 0.8	160.0 ± 332.0	0.00 ± 0.01	3.32 ± 0.42	0.3 ± 0.8
DENS2_199	8.0 ± 0.4	5.0 ± 1.4	19.0 ± 61.9	0.07 ± 0.03	3.86 ± 0.51	<2.5
DENS2_202	8.5 ± 0.2	8.2 ± 3.8	40.0 ± 33.5	0.01 ± 0.01	4.96 ± 0.43	1.6 ± 1.1
DENS2_235	7.8 ± 1.0	4.5 ± 1.9	15.0 ± 209.9	0.09 ± 0.04	5.08 ± 0.44	<2.5
DENS3_17	7.2 ± 0.6	1.6 ± 0.6	10.0 ± 50.6	0.00 ± 0.03	1.62 ± 0.42	4.6 ± 0.9
DENS3_41	8.8 ± 0.2	22.2 ± 8.4	30.0 ± 28.3	0.09 ± 0.02	1.85 ± 0.39	<3.3
DENS3_118	9.0 ± 0.4	2.8 ± 1.9	321.0 ± 523.5	0.06 ± 0.04	2.75 ± 0.41	0.8 ± 1.1
DENS3_285	8.3 ± 0.4	2.0 ± 1.6	101.0 ± 143.6	0.00 ± 0.02	2.14 ± 0.43	3.9 ± 1.1
FIELD1_45	9.0 ± 0.2	7.1 ± 2.3	127.0 ± 89.8	0.04 ± 0.02	9.77 ± 0.56	5.4 ± 1.1
FIELD1_89	8.5 ± 0.6	1.5 ± 1.2	202.0 ± 433.8	0.01 ± 0.03	3.16 ± 0.43	<3.4
FIELD1_122	7.7 ± 0.1	4.7 ± 1.0	10.0 ± 2.3	0.03 ± 0.02	5.60 ± 0.47	<2.8
FIELD1_180	8.7 ± 0.2	18.1 ± 6.0	30.0 ± 30.3	0.07 ± 0.01	5.70 ± 0.44	6.9 ± 1.1
FIELD1_265	8.0 ± 0.4	5.4 ± 1.0	19.0 ± 49.2	0.04 ± 0.02	2.93 ± 0.51	9.4 ± 1.1
FIELD1_281	7.9 ± 0.3	4.4 ± 1.8	19.0 ± 29.9	0.10 ± 0.05	2.70 ± 0.42	0.3 ± 0.9
FIELD2_64	8.7 ± 0.1	23.7 ± 3.3	19.0 ± 7.9	0.12 ± 0.02	1.71 ± 0.52	2.4 ± 1.1
FIELD2_91	8.5 ± 0.3	19.6 ± 6.0	15.0 ± 30.1	0.08 ± 0.02	5.62 ± 0.53	2.6 ± 1.2
FIELD2_132	9.0 ± 0.2	8.0 ± 2.1	127.0 ± 78.8	0.04 ± 0.02	3.42 ± 0.54	6.1 ± 1.2
FIELD2_174	9.1 ± 0.1	19.0 ± 7.9	64.0 ± 34.6	0.04 ± 0.01	6.72 ± 0.54	11.4 ± 1.2
FIELD3_124	8.1 ± 0.7	7.9 ± 1.9	15.0 ± 80.4	0.04 ± 0.02	5.66 ± 0.56	<3.7
FIELD3_327	7.7 ± 0.6	4.8 ± 1.1	10.0 ± 47.3	0.02 ± 0.02	2.62 ± 0.45	0.4 ± 0.8
FIELD4_33	8.3 ± 0.2	9.2 ± 2.3	19.0 ± 17.0	0.05 ± 0.02	6.98 ± 0.49	7.0 ± 1.1
FIELD4_50	8.6 ± 0.3	19.9 ± 4.7	19.0 ± 43.0	0.13 ± 0.03	3.11 ± 0.48	3.2 ± 1.1
FIELD4_124	9.6 ± 0.1	5.0 ± 0.4	806.0 ± 324.8	0.00 ± 0.00	31.67 ± 0.80	<3.5
			*p*LAEs			
DENS1_43	8.5 ± 0.2	14.2 ± 5.3	19.0 ± 19.7	0.20 ± 0.06	1.26 ± 0.38	<2.5
DENS1_59	9.5 ± 0.2	24.6 ± 16.3	127.0 ± 212.2	0.26 ± 0.06	1.59 ± 0.38	3.4 ± 1.1
DENS1_97	8.5 ± 0.1	17.5 ± 3.4	19.0 ± 0.0	0.16 ± 0.04	1.76 ± 0.39	<3.3
DENS1_143	8.3 ± 1.0	1.1 ± 1.9	160.0 ± 597.8	0.02 ± 0.04	0.95 ± 0.40	1.8 ± 1.1
DENS1_172	9.0 ± 0.4	8.2 ± 5.6	127.0 ± 344.1	0.10 ± 0.04	1.71 ± 0.45	4.1 ± 1.1
DENS1_235	9.3 ± 0.2	12.0 ± 3.8	160.0 ± 134.5	0.10 ± 0.02	1.82 ± 0.40	<3.4
DENS1_245	8.8 ± 0.3	12.7 ± 5.4	50.0 ± 81.0	0.11 ± 0.02	2.22 ± 0.40	<3.3
DENS1_266	9.3 ± 0.2	4.4 ± 1.9	508.0 ± 470.6	0.04 ± 0.03	1.02 ± 0.41	1.3 ± 1.1
DENS1_304	7.4 ± 2.2	2.7 ± 2.2	10.0 ± 165.8	0.07 ± 0.08	1.28 ± 0.54	1.2 ± 1.1
DENS1_344	8.4 ± 0.6	2.7 ± 2.0	101.0 ± 260.3	0.03 ± 0.03	3.25 ± 0.44	2.6 ± 1.1
DENS2_24	8.7 ± 0.1	23.4 ± 3.1	19.0 ± 6.1	0.15 ± 0.02	1.74 ± 0.42	1.8 ± 1.1
DENS2_239	8.7 ± 0.3	6.8 ± 4.6	80.0 ± 193.5	0.15 ± 0.05	2.20 ± 0.40	<3.3
DENS2_281	8.3 ± 0.2	9.6 ± 2.4	19.0 ± 15.4	0.06 ± 0.02	2.04 ± 0.42	4.7 ± 1.1
DENS3_20	8.9 ± 0.0	37.3 ± 3.6	19.0 ± 0.0	0.16 ± 0.02	1.11 ± 0.39	<3.4
DENS3_126	9.1 ± 0.1	26.0 ± 7.4	50.0 ± 34.6	0.15 ± 0.02	2.08 ± 0.39	0.7 ± 1.1
DENS3_172	8.8 ± 0.5	1.1 ± 1.6	508.0 ± 696.7	0.01 ± 0.03	2.09 ± 0.42	0.4 ± 1.1
DENS3_279	9.3 ± 0.2	1.9 ± 0.6	1015.0 ± 661.0	0.03 ± 0.03	1.68 ± 0.40	<2.5
FIELD1_60	8.5 ± 0.1	16.4 ± 3.4	19.0 ± 2.5	0.13 ± 0.03	1.51 ± 0.41	<3.3
FIELD1_71	8.5 ± 0.1	16.6 ± 4.6	19.0 ± 1.1	0.13 ± 0.05	1.44 ± 0.43	2.7 ± 1.1
FIELD1_270	9.6 ± 0.1	25.8 ± 8.4	160.0 ± 86.3	0.18 ± 0.03	1.65 ± 0.41	9.2 ± 1.1
FIELD1_283	9.3 ± 0.1	83.3 ± 12.1	25.0 ± 7.1	0.14 ± 0.01	3.89 ± 0.91	28.0 ± 1.2
FIELD2_26	8.4 ± 0.5	5.4 ± 3.0	50.0 ± 113.7	0.04 ± 0.02	3.29 ± 0.54	1.9 ± 1.1
FIELD2_29	9.1 ± 0.2	15.5 ± 7.3	80.0 ± 51.2	0.11 ± 0.02	1.73 ± 0.51	2.6 ± 1.1
FIELD2_71	8.7 ± 0.1	28.0 ± 4.9	19.0 ± 1.7	0.16 ± 0.03	1.70 ± 0.50	4.1 ± 1.1
FIELD2_116	8.4 ± 0.1	13.6 ± 3.8	19.0 ± 11.4	0.13 ± 0.04	1.35 ± 0.51	<3.3
FIELD2_140	9.5 ± 0.1	71.6 ± 17.0	40.0 ± 23.7	0.16 ± 0.01	2.79 ± 0.50	<3.5
FIELD2_141	8.8 ± 0.1	28.6 ± 4.0	19.0 ± 11.0	0.12 ± 0.01	2.47 ± 0.50	<3.4
FIELD2_149	8.2 ± 0.3	8.1 ± 4.6	19.0 ± 15.4	0.15 ± 0.10	2.85 ± 0.26	5.4 ± 1.1
FIELD2_181	8.9 ± 0.0	37.0 ± 4.7	19.0 ± 3.7	0.16 ± 0.02	1.99 ± 0.50	2.1 ± 1.1
FIELD2_243	8.8 ± 0.0	28.6 ± 2.9	19.0 ± 0.9	0.13 ± 0.02	2.30 ± 0.50	6.3 ± 1.1
FIELD2_253	9.3 ± 0.1	24.0 ± 9.3	80.0 ± 52.1	0.17 ± 0.03	1.60 ± 0.51	<3.3
FIELD2_257	8.7 ± 0.1	26.9 ± 3.5	19.0 ± 3.4	0.12 ± 0.01	2.16 ± 0.50	1.4 ± 1.1
FIELD3_173	8.3 ± 0.4	10.9 ± 2.4	19.0 ± 46.7	0.08 ± 0.02	4.10 ± 0.44	<3.5
FIELD3_311	8.6 ± 0.1	20.4 ± 3.5	19.0 ± 2.0	0.14 ± 0.03	2.20 ± 0.47	<3.3
FIELD4_127	8.5 ± 0.4	10.4 ± 4.1	30.0 ± 64.0	0.05 ± 0.02	3.00 ± 0.51	0.3 ± 1.1

Table 6
Properties of the LAEs

ID	r_e (kpc)	$\Sigma_{\rm SFR}$ ($M_\odot$ yr^{-1} kpc^{-2})	$\Sigma_{\rm sSFR}$ (Gyr^{-1} kpc^{-2})
		*z*LAEs	
DENS1_86	<1.0	>0.12	>1.53
DENS1_290	<1.0	>0.38	>15.57
DENS1_306	<1.0	>2.26	>7.76
DENS1_339	<1.0	>1.78	>15.57
DENS1_356	<1.0	>0.17	>0.96
DENS2_199	<1.0	>0.78	>7.77
DENS2_202	2.2 ± 0.2	0.26 ± 0.08	0.81 ± 0.48
DENS2_235	<1.0	>0.70	>10.23
DENS3_17	<1.0	>0.25	>15.49
DENS3_41	<1.0	>3.42	>5.12
DENS3_118	<1.0	>0.43	>0.48
DENS3_285	<1.0	>0.30	>1.52
FIELD1_45	<1.0	>1.11	>1.21
FIELD1_89	<1.0	>0.23	>0.77
FIELD1_122	<1.0	>0.73	>15.65
FIELD1_180	1.5 ± 0.1	1.24 ± 0.19	2.30 ± 1.22
FIELD1_265	<1.0	>0.84	>7.81
FIELD1_281	<1.0	>0.69	>7.80
FIELD2_64	<1.0	>3.68	>7.79
FIELD2_91	2.4 ± 0.2	0.56 ± 0.09	1.89 ± 1.45
FIELD2_132	2.2 ± 0.2	0.27 ± 0.03	0.26 ± 0.10
FIELD2_174	<1.0	>2.96	>2.44
FIELD3_124	<1.0	>1.24	>10.38
FIELD3_327	<1.0	>0.74	>15.31
FIELD4_33	<1.0	>1.41	>7.71
FIELD4_50	4.1 ± 0.3	0.19 ± 0.02	0.47 ± 0.33
FIELD4_124	<1.0	>0.77	>0.19
		*p*LAEs	
DENS1_43	1.8 ± 0.3	0.70 ± 0.00	2.47 ± 1.08
DENS1_59	1.6 ± 0.2	1.46 ± 0.64	0.47 ± 0.29
DENS1_97	2.3 ± 0.3	0.52 ± 0.03	1.49 ± 0.30
DENS1_143	<1.0	>0.17	>0.96
DENS1_172	6.0 ± 0.8	0.04 ± 0.02	0.03 ± 0.04
DENS1_235	<1.0	>1.86	>0.96
DENS1_245	<1.0	>1.97	>3.09
DENS1_266	<1.0	>0.68	>0.30
DENS1_304	<1.0	>0.41	>15.46
DENS1_344	<1.0	>0.42	>1.52
DENS2_24	2.4 ± 0.2	0.66 ± 0.00	1.41 ± 0.25
DENS2_239	2.7 ± 0.3	0.15 ± 0.06	0.28 ± 0.25
DENS2_281	1.8 ± 0.2	0.48 ± 0.00	2.50 ± 0.91
DENS3_20	2.5 ± 0.1	0.93 ± 0.00	1.25 ± 0.12
DENS3_126	<1.0	>4.02	>3.09
DENS3_172	<1.0	>0.18	>0.30
DENS3_279	2.0 ± 0.3	0.07 ± 0.00	0.04 ± 0.02
FIELD1_60	2.2 ± 0.2	0.56 ± 0.01	1.70 ± 0.28
FIELD1_71	2.1 ± 0.2	0.60 ± 0.05	1.81 ± 0.54
FIELD1_270	2.2 ± 0.1	0.84 ± 0.18	0.20 ± 0.07
FIELD1_283	1.4 ± 0.1	6.79 ± 0.22	3.25 ± 0.53
FIELD2_26	<1.0	>0.83	>3.09
FIELD2_29	<1.0	>2.39	>1.92
FIELD2_71	3.6 ± 0.2	0.34 ± 0.02	0.61 ± 0.09
FIELD2_116	2.0 ± 0.2	0.52 ± 0.03	1.92 ± 0.54
FIELD2_140	1.3 ± 0.1	6.92 ± 0.77	2.42 ± 0.76
FIELD2_141	1.7 ± 0.1	1.61 ± 0.00	2.82 ± 0.68
FIELD2_149	<1.0	>1.25	>7.75
FIELD2_181	2.6 ± 0.1	0.89 ± 0.03	1.20 ± 0.14
FIELD2_243	3.1 ± 0.1	0.49 ± 0.00	0.85 ± 0.09
FIELD2_253	3.2 ± 0.2	0.37 ± 0.10	0.19 ± 0.08
FIELD2_257	<1.0	>4.15	>7.75
FIELD3_173	<1.0	>1.69	>7.75
FIELD3_311	2.5 ± 0.2	0.52 ± 0.00	1.27 ± 0.20
FIELD4_127	1.8 ± 0.2	0.51 ± 0.09	1.65 ± 1.44

Table 7
Lyα Escape Proxies for the LAEs

ID	$W_{\rm Ly\alpha}$ (Å)	Lyα/[O II]	$f_{\rm esc}^{\rm Ly\alpha}$
		*z*LAEs	
DENS1_86	188.2 ± 81.36	>12.11	1.67 ± 1.54
DENS1_290	95.0 ± 38.25	8.15 ± 2.54	0.49 ± 0.28
DENS1_306	43.4 ± 7.37	4.48 ± 0.94	0.09 ± 0.02
DENS1_339	77.2 ± 18.31	>11.50	0.12 ± 0.03
DENS1_356	143.1 ± 42.82	98.04 ± 240.63	1.36 ± 1.00
DENS2_199	201.4 ± 89.15	>15.55	0.34 ± 0.11
DENS2_202	40.8 ± 4.42	31.98 ± 22.79	0.27 ± 0.13
DENS2_235	232.4 ± 59.34	>20.59	0.50 ± 0.21
DENS3_17	81.3 ± 34.00	3.50 ± 1.12	0.44 ± 0.20
DENS3_41	22.5 ± 5.20	>5.59	0.04 ± 0.02
DENS3_118	127.1 ± 38.41	36.00 ± 52.07	0.44 ± 0.31
DENS3_285	57.9 ± 16.52	5.41 ± 1.84	0.48 ± 0.40
FIELD1_45	154.9 ± 26.59	18.25 ± 4.01	0.61 ± 0.20
FIELD1_89	142.3 ± 42.19	>9.24	0.97 ± 0.79
FIELD1_122	143.1 ± 27.77	>20.26	0.54 ± 0.12
FIELD1_180	64.7 ± 7.48	8.21 ± 1.48	0.14 ± 0.05
FIELD1_265	112.5 ± 43.58	3.12 ± 0.66	0.24 ± 0.06
FIELD1_281	192.7 ± 72.70	78.96 ± 204.40	0.27 ± 0.12
FIELD2_64	39.6 ± 14.13	7.00 ± 3.92	0.03 ± 0.01
FIELD2_91	67.7 ± 8.97	21.66 ± 9.85	0.13 ± 0.04
FIELD2_132	48.7 ± 9.72	5.61 ± 1.39	0.19 ± 0.06
FIELD2_174	38.3 ± 3.72	5.88 ± 0.76	0.16 ± 0.07
FIELD3_124	137.5 ± 34.43	>15.46	0.32 ± 0.08
FIELD3_327	86.0 ± 24.95	60.42 ± 111.36	0.24 ± 0.07
FIELD4_33	115.1 ± 15.58	9.99 ± 1.71	0.34 ± 0.09
FIELD4_50	89.6 ± 22.19	9.62 ± 3.56	0.07 ± 0.02
FIELD4_124	303.1 ± 41.55	>90.80	2.85 ± 0.22
		*p*LAEs	
DENS1_43	143.5 ± 83.51	>5.04	0.04 ± 0.02
DENS1_59	146.5 ± 71.37	4.72 ± 1.93	0.03 ± 0.02
DENS1_97	123.4 ± 51.16	>5.37	0.04 ± 0.01
DENS1_143	61.3 ± 38.22	5.30 ± 3.99	0.38 ± 0.66
DENS1_172	64.4 ± 27.43	4.21 ± 1.60	0.09 ± 0.07
DENS1_235	40.1 ± 11.28	>5.31	0.07 ± 0.03
DENS1_245	68.5 ± 19.03	>6.68	0.08 ± 0.04
DENS1_266	21.7 ± 10.19	7.76 ± 7.30	0.10 ± 0.06
DENS1_304	111.2 ± 114.88	10.25 ± 10.05	0.21 ± 0.20
DENS1_344	135.4 ± 42.92	12.53 ± 5.65	0.53 ± 0.40
DENS2_24	74.7 ± 25.32	9.71 ± 6.56	0.03 ± 0.01
DENS2_239	157.0 ± 51.91	>6.71	0.15 ± 0.10
DENS2_281	41.5 ± 10.50	4.34 ± 1.38	0.09 ± 0.03
DENS3_20	38.2 ± 15.68	>3.24	0.01 ± 0.00
DENS3_126	52.8 ± 12.22	29.97 ± 48.80	0.04 ± 0.01
DENS3_172	113.8 ± 42.65	50.77 ± 134.47	0.82 ± 1.16
DENS3_279	74.6 ± 26.48	>6.75	0.39 ± 0.16
FIELD1_60	65.7 ± 26.12	>4.58	0.04 ± 0.01
FIELD1_71	105.6 ± 58.71	5.33 ± 2.71	0.04 ± 0.02
FIELD1_270	54.9 ± 17.95	1.79 ± 0.49	0.03 ± 0.01
FIELD1_283	30.9 ± 7.52	1.39 ± 0.33	0.02 ± 0.01
FIELD2_26	65.6 ± 15.56	17.09 ± 10.15	0.27 ± 0.16
FIELD2_29	34.9 ± 11.93	6.53 ± 3.37	0.05 ± 0.03
FIELD2_71	68.1 ± 26.40	4.14 ± 1.67	0.03 ± 0.01
FIELD2_116	61.7 ± 30.98	>4.08	0.04 ± 0.02
FIELD2_140	32.3 ± 6.52	>8.00	0.02 ± 0.01
FIELD2_141	52.0 ± 13.08	>7.31	0.04 ± 0.01
FIELD2_149	858.0 ± 565.77	5.25 ± 1.16	0.16 ± 0.09
FIELD2_181	51.7 ± 16.06	9.58 ± 5.72	0.02 ± 0.01
FIELD2_243	59.4 ± 16.52	3.63 ± 1.00	0.04 ± 0.01
FIELD2_253	49.7 ± 19.57	>4.88	0.03 ± 0.01
FIELD2_257	45.8 ± 12.82	15.11 ± 12.01	0.04 ± 0.01
FIELD3_173	121.5 ± 24.68	>11.77	0.17 ± 0.04
FIELD3_311	136.4 ± 63.59	>6.72	0.05 ± 0.01
FIELD4_127	42.8 ± 9.40	115.28 ± 492.40	0.13 ± 0.06

ORCID iDs

Ragadeepika Pucha https://orcid.org/0000-0002-4940-3009
Naveen A. Reddy https://orcid.org/0000-0001-9687-4973
Arjun Dey https://orcid.org/0000-0002-4928-4003
Stéphanie Juneau https://orcid.org/0000-0002-0000-2394
Kyoung-Soo Lee https://orcid.org/0000-0003-3004-9596
Moire K. M. Prescott https://orcid.org/0000-0001-8302-0565
Irene Shivaei https://orcid.org/0000-0003-4702-7561
Sungryong Hong https://orcid.org/0000-0001-9991-8222

References

Acquaviva, V., Vargas, C., Gawiser, E., & Guaita, L. 2012, ApJL, 751, L26
Adams, J. J., Blanc, G. A., Hill, G. J., et al. 2011, ApJS, 192, 5
Arrabal Haro, P., Rodríguez Espinosa, J. M., Muñoz-Tuñón, C., et al. 2018, MNRAS, 478, 3740
Arrabal Haro, P., Rodríguez Espinosa, J. M., Muñoz-Tuñón, C., et al. 2020, MNRAS, 495, 1807
Avila, R. J., Hack, W. J. & STScI AstroDrizzle Team 2012, AAS Meeting, 220, 135.13
Bacon, R., Conseil, S., Mary, D., et al. 2017, A&A, 608, A1
Bertin, E., & Arnouts, S. 1996, A&AS, 117, 393
Blanc, G. A., Adams, J. J., Gebhardt, K., et al. 2011, ApJ, 736, 31
Bond, N. A., Gawiser, E., Gronwall, C., et al. 2009, ApJ, 705, 639
Bond, N. A., Gawiser, E., Guaita, L., et al. 2012, ApJ, 753, 95
Borthakur, S., Heckman, T. M., Leitherer, C., & Overzier, R. A. 2014, Sci, 346, 216
Bradley, L., Sipőcz, B., Robitaille, T., et al. 2019, astropy/photutils: v0.6, Zenodo, doi:10.5281/zenodo.2533376
Brinchmann, J., Charlot, S., White, S. D. M., et al. 2004, MNRAS, 351, 1151
Bruzual, G., & Charlot, S. 2003, MNRAS, 344, 1000
Carnall, A. C., McLure, R. J., Dunlop, J. S., & Davé, R. 2018, MNRAS, 480, 4379
Cen, R. 2020, ApJL, 889, L22
Chabrier, G. 2003, PASP, 115, 763
Cullen, F., McLure, R. J., Dunlop, J. S., et al. 2020, MNRAS, 495, 1501
Daddi, E., Dickinson, M., Morrison, G., et al. 2007, ApJ, 670, 156
De Barros, S., Pentericci, L., Vanzella, E., et al. 2017, A&A, 608, A123
Dey, A., Bian, C., Soifer, B. T., et al. 2005, ApJ, 629, 654
Dey, A., Lee, K.-S., Reddy, N., et al. 2016, ApJ, 823, 11
Dijkstra, M. 2017, arXiv:1704.03416
Dressel, L. 2012, Wide Field Camera 3 Instrument Handbook for Cycle 21 v. 5.0
Du, X., Shapley, A. E., Reddy, N. A., et al. 2018, ApJ, 860, 75
Du, X., Shapley, A. E., Topping, M. W., et al. 2021, ApJ, 920, 95
Elbaz, D., Daddi, E., Le Borgne, D., et al. 2007, A&A, 468, 33
Eldridge, J. J., Stanway, E. R., Xiao, L., et al. 2017, PASA, 34, e058
Fabricant, D., Fata, R., Roll, J., et al. 2005, PASP, 117, 1411
Ferland, G. J., Porter, R. L., van Hoof, P. A. M., et al. 2013, RMxAA, 49, 137
Finkelstein, S. L., Cohen, S. H., Moustakas, J., et al. 2011, ApJ, 733, 117
Finkelstein, S. L., Rhoads, J. E., Malhotra, S., & Grogin, N. 2009, ApJ, 691, 465
Finkelstein, S. L., Rhoads, J. E., Malhotra, S., Pirzkal, N., & Wang, J. 2007, ApJ, 660, 1023
Gawiser, E., Francke, H., Lai, K., et al. 2007, ApJ, 671, 278
Gawiser, E., van Dokkum, P. G., Gronwall, C., et al. 2006, ApJL, 642, L13
Giardino, G., de Oliveira, C. A., Arribas, S., et al. 2016, in ASP Conf. Ser. 507, Multi-Object Spectroscopy in the Next Decade: Big Questions, Large Surveys, and Wide Fields, ed. I. Skillen, M. Balcells, & S. Trager (San Francisco, CA: ASP), 305
Giavalisco, M. 2002, ARA&A, 40, 579
Gnedin, N. Y., Kravtsov, A. V., & Chen, H.-W. 2008, ApJ, 672, 765
Gordon, K. D., Clayton, G. C., Misselt, K. A., Landolt, A. U., & Wolff, M. J. 2003, ApJ, 594, 279
Grogin, N. A., Kocevski, D. D., Faber, S. M., et al. 2011, ApJS, 197, 35
Gronwall, C., Bond, N. A., Ciardullo, R., et al. 2011, ApJ, 743, 9
Guaita, L., Acquaviva, V., Padilla, N., et al. 2011, ApJ, 733, 114
Hagen, A., Ciardullo, R., Gronwall, C., et al. 2014, ApJ, 786, 59
Hagen, A., Zeimann, G. R., Behrens, C., et al. 2016, ApJ, 817, 79
Hao, C.-N., Huang, J.-S., Xia, X., et al. 2018, ApJ, 864, 145
Hathi, N. P., Le Fèvre, O., Ilbert, O., et al. 2016, A&A, 588, A26
Hayes, M., Östlin, G., Schaerer, D., et al. 2010, Natur, 464, 562
Hayes, M., Schaerer, D., Östlin, G., et al. 2011, ApJ, 730, 8
Heckman, T. M., Borthakur, S., Overzier, R., et al. 2011, ApJ, 730, 5
Herenz, E. C., Hayes, M., & Scarlata, C. 2020, A&A, 642, A55
Herrero Alonso, Y., Krumpe, M., Wisotzki, L., et al. 2021, A&A, 653, A136
Hinshaw, G., Larson, D., Komatsu, E., et al. 2013, ApJS, 208, 19
Hoag, A., Treu, T., Pentericci, L., et al. 2019, MNRAS, 488, 706
Hong, S., Dey, A., & Prescott, M. K. M. 2014, PASP, 126, 1048
Huang, Y., Lee, K.-S., Shi, K., et al. 2021, ApJ, 921, 4
Izotov, Y. I., Orlitová, I., Schaerer, D., et al. 2016, Natur, 529, 178
Jannuzi, B. T., & Dey, A. 1999, in ASP Conf. Ser. 191, Photometric Redshifts and the Detection of High Redshift Galaxies, ed. R. Weymann et al. (San Francisco, CA: ASP), 111
Jaskot, A. E., Dowd, T., Oey, M. S., Scarlata, C., & McKinney, J. 2019, ApJ, 885, 96
Jiang, L., Egami, E., Fan, X., et al. 2013, ApJ, 773, 153
Ivezić, Ž, Kahn, S. M., Tyson, J. A., et al. 2019, ApJ, 873, 111
Kakiichi, K., & Gronke, M. 2021, ApJ, 908, 30
Kashino, D., Lilly, S. J., Renzini, A., et al. 2022, ApJ, 925, 82
Khostovan, A. A., Sobral, D., Mobasher, B., et al. 2019, MNRAS, 489, 555
Kim, K., Malhotra, S., Rhoads, J. E., Butler, N. R., & Yang, H. 2020, ApJ, 893, 134
Kim, K. J., Malhotra, S., Rhoads, J. E., & Yang, H. 2021, ApJ, 914, 2
Kimm, T., Blaizot, J., Garel, T., et al. 2019, MNRAS, 486, 2215
Knapen, J. H., & Cisternas, M. 2015, ApJL, 807, L16
Koekemoer, A. M., Faber, S. M., Ferguson, H. C., et al. 2011, ApJS, 197, 36
Kornei, K. A., Shapley, A. E., Erb, D. K., et al. 2010, ApJ, 711, 693
Kriek, M., Shapley, A. E., Reddy, N. A., et al. 2015, ApJS, 218, 15
Kusakabe, H., Shimasaku, K., Ouchi, M., et al. 2018, PASJ, 70, 4
Lai, K., Huang, J.-S., Fazio, G., et al. 2008, ApJ, 674, 70
Law, D. R., Steidel, C. C., Shapley, A. E., et al. 2012, ApJ, 745, 85
Leclercq, F., Bacon, R., Verhamme, A., et al. 2020, A&A, 635, A82
Leitherer, C., & Heckman, T. M. 1995, ApJS, 96, 9
Lemaux, B. C., Fuller, S., Bradač, M., et al. 2021, MNRAS, 504, 3662
Lemaux, B. C., Le Fèvre, O., Cucciati, O., et al. 2018, A&A, 615, A77
Luo, W., Yang, X., & Zhang, Y. 2014, ApJL, 789, L16
Ma, X., Hopkins, P. F., Kasen, D., et al. 2016, MNRAS, 459, 3614
Ma, X., Quataert, E., Wetzel, A., et al. 2020, MNRAS, 498, 2001
Malavasi, N., Lee, K.-S., Dey, A., et al. 2021, ApJ, 921, 103
Malhotra, S., Rhoads, J. E., Finkelstein, S. L., et al. 2012, ApJL, 750, L36
Marchi, F., Pentericci, L., Guaita, L., et al. 2017, A&A, 601, A73
Marchi, F., Pentericci, L., Guaita, L., et al. 2018, A&A, 614, A11
Marchi, F., Pentericci, L., Guaita, L., et al. 2019, A&A, 631, A19
Matthee, J., Sobral, D., Hayes, M., et al. 2021, MNRAS, 505, 1382
Matthee, J., Sobral, D., Oteo, I., et al. 2016, MNRAS, 458, 449
McLean, I. S., Steidel, C. C., Epps, H. W., et al. 2012, Proc. SPIE, 8446, 84460J
McLinden, E. M., Rhoads, J. E., Malhotra, S., et al. 2014, MNRAS, 439, 446
Miyazaki, S., Komiyama, Y., Sekiguchi, M., et al. 2002, PASJ, 54, 833
Momose, R., Ouchi, M., Nakajima, K., et al. 2014, MNRAS, 442, 110
Moreno, J., Torrey, P., Ellison, S. L., et al. 2021, MNRAS, 503, 3113
Naidu, R. P., Matthee, J., Oesch, P. A., et al. 2022, MNRAS, 510, 4582
Naidu, R. P., Tacchella, S., Mason, C. A., et al. 2020, ApJ, 892, 109
Nakajima, K., Ouchi, M., Shimasaku, K., et al. 2012, ApJ, 745, 12
Nakajima, K., Ouchi, M., Shimasaku, K., et al. 2013, ApJ, 769, 3
Nilsson, K. K., Møller, P., Möller, O., et al. 2007, A&A, 471, 71
Nilsson, K. K., Östlin, G., Møller, P., et al. 2011, A&A, 529, A9
Noeske, K. G., Faber, S. M., Weiner, B. J., et al. 2007, ApJL, 660, L47
Oke, J. B., Cohen, J. G., Carr, M., et al. 1995, PASP, 107, 375
Oke, J. B., & Gunn, J. E. 1983, ApJ, 266, 713
Ono, Y., Ouchi, M., Shimasaku, K., et al. 2010, MNRAS, 402, 1580
Ouchi, M., Ono, Y., & Shibuya, T. 2020, ARA&A, 58, 617
Ouchi, M., Shimasaku, K., Furusawa, H., et al. 2003, ApJ, 582, 60
Oyarzún, G. A., Blanc, G. A., González, V., et al. 2016, ApJL, 821, L14
Oyarzún, G. A., Blanc, G. A., González, V., Mateo, M., & Bailey, J. I. I. 2017, ApJ, 843, 133
Pahl, A. J., Shapley, A., Steidel, C. C., Chen, Y., & Reddy, N. A. 2021, MNRAS, 505, 2447
Partridge, R. B., & Peebles, P. J. E. 1967, ApJ, 147, 868
Paulino-Afonso, A., Sobral, D., Ribeiro, B., et al. 2018, MNRAS, 476, 5479
Peng, C. Y., Ho, L. C., Impey, C. D., & Rix, H.-W. 2010, AJ, 139, 2097
Pentericci, L., Grazian, A., Fontana, A., et al. 2007, A&A, 471, 433
Pentericci, L., Grazian, A., Fontana, A., et al. 2009, A&A, 494, 553
Pérez-Montero, E. 2014, MNRAS, 441, 2663
Pirzkal, N., Malhotra, S., Rhoads, J. E., & Xu, C. 2007, ApJ, 667, 49
Pirzkal, N., Viana, A., & Rajan, A. 2010, The WFC3 IR 'Blobs", Space Telescope WFC Instrument Science Report

Prescott, M. K. M., Kashikawa, N., Dey, A., & Matsuda, Y. 2008, ApJL, 678, L77
Razoumov, A. O., & Sommer-Larsen, J. 2010, ApJ, 710, 1239
Reddy, N. A., Kriek, M., Shapley, A. E., et al. 2015, ApJ, 806, 259
Reddy, N. A., Oesch, P. A., Bouwens, R. J., et al. 2018b, ApJ, 853, 56
Reddy, N. A., Shapley, A. E., Sanders, R. L., et al. 2018a, ApJ, 869, 92
Reddy, N. A., Steidel, C. C., Pettini, M., Bogosavljević, M., & Shapley, A. E. 2016, ApJ, 828, 108
Reddy, N. A., Topping, M. W., Shapley, A. E., et al. 2022, ApJ, 926, 31
Rhoads, J. E., Malhotra, S., Dey, A., et al. 2000, ApJL, 545, L85
Rivera-Thorsen, T. E., Hayes, M., Östlin, G., et al. 2015, ApJ, 805, 14
Salpeter, E. E. 1955, ApJ, 121, 161
Sandberg, A., Guaita, L., Östlin, G., Hayes, M., & Kiaeerad, F. 2015, A&A, 580, A91
Sanderson, K. N., Prescott, M. K. M., Christensen, L., Fynbo, J., & Møller, P. 2021, ApJ, 923, 252
Santos, S., Sobral, D., Matthee, J., et al. 2020, MNRAS, 493, 141
Schreiber, C., Pannella, M., Elbaz, D., et al. 2015, A&A, 575, A74
Sérsic, J. L. 1963, BAAA, 6, 41
Sharma, M., Theuns, T., Frenk, C., et al. 2016, MNRAS, 458, L94
Shi, K., Huang, Y., Lee, K.-S., et al. 2019, ApJ, 879, 9
Shi, K., Toshikawa, J., Cai, Z., Lee, K.-S., & Fang, T. 2020, ApJ, 899, 79
Shibuya, T., Ouchi, M., & Harikane, Y. 2015, ApJS, 219, 15
Shibuya, T., Ouchi, M., Harikane, Y., & Nakajima, K. 2019, ApJ, 871, 164
Shimakawa, R., Kodama, T., Shibuya, T., et al. 2017, MNRAS, 468, 1123
Shivaei, I., Reddy, N., Rieke, G., et al. 2020, ApJ, 899, 117
Shivaei, I., Reddy, N. A., Shapley, A. E., et al. 2015, ApJ, 815, 98
Sobral, D., & Matthee, J. 2019, A&A, 623, A157
Sobral, D., Matthee, J., Best, P., et al. 2017, MNRAS, 466, 1242
Sobral, D., Matthee, J., Darvish, B., et al. 2018, MNRAS, 477, 2817
Song, M., Finkelstein, S. L., Gebhardt, K., et al. 2014, ApJ, 791, 3
Steidel, C. C., Bogosavljević, M., Shapley, A. E., et al. 2011, ApJ, 736, 160
Steidel, C. C., Bogosavljević, M., Shapley, A. E., et al. 2018, ApJ, 869, 123
Steidel, C. C., & Hamilton, D. 1993, AJ, 105, 2017
Steidel, C. C., Strom, A. L., Pettini, M., et al. 2016, ApJ, 826, 159
Stierwalt, S., Besla, G., Patton, D., et al. 2015, ApJ, 805, 2
Sunnquist, B. 2018, WFC3/IR Blob Monitoring, Space Telescope WFC Instrument Science Report
Tody, D. 1993, in ASP Conf. Ser. 52, Astronomical Data Analysis Software and Systems II, ed. R. J. Hanisch, R. J. V. Brissenden, & J. Barnes (San Francisco, CA: ASP), 173
Topping, M. W., Shapley, A. E., Reddy, N. A., et al. 2020a, MNRAS, 495, 4430
Topping, M. W., Shapley, A. E., Reddy, N. A., et al. 2020b, MNRAS, 499, 1652
Trainor, R. F., Steidel, C. C., Strom, A. L., & Rudie, G. C. 2015, ApJ, 809, 89
Vargas, C. J., Bish, H., Acquaviva, V., et al. 2014, ApJ, 783, 26
Verhamme, A., Orlitová, I., Schaerer, D., et al. 2017, A&A, 597, A13
Weiss, L. H., Bowman, W. P., Ciardullo, R., et al. 2021, ApJ, 912, 100
Whitaker, K. E., Franx, M., Leja, J., et al. 2014, ApJ, 795, 104
Wisotzki, L., Bacon, R., Brinchmann, J., et al. 2018, Natur, 562, 229
Wofford, A., Leitherer, C., & Salzer, J. 2013, ApJ, 765, 118
Yang, H., Malhotra, S., Gronke, M., et al. 2017, ApJ, 844, 171
Zhang, Y., Ouchi, M., Gebhardt, K., et al. 2021, ApJ, 922, 167